Additive Manufacturing 73 (2023) 103679

Contents lists available at ScienceDirect

Additive Manufacturing

journal homepage: www.elsevier.com/locate/addma

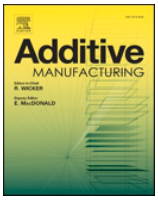

Electrical capability of 3D printed unpoled polyvinylidene fluoride (PVDF)/ thermoplastic polyurethane (TPU) sensors combined with carbon black and barium titanate

Dejana Pejak Simunec *, Michael Breedon, Faizan U.R. Muhammad, Louis Kyratzis, Antonella Sola

Commonwealth Scientific and Industrial Research Organisation (CSIRO), Manufacturing Business Unit Research Way, Melbourne, VIC 3168, Australia

ARTICLE INFO

Keywords:
Fused deposition modelling
FDM
Fused filament fabrication
FFF
Electrical conductivity
Composite material
Additive manufacturing
Sensor
Piezoelectricity

ABSTRACT

The development of three-dimensional (3D) printed sensors attracts high interest from the smart electronic industry owing to the significant geometric freedom allowed by the printing process and the potential for bespoke composite feedstocks being imbued with specific material properties. In particular, feedstock for material extrusion (MEX) additive manufacturing by fused filament fabrication can be provided with piezoelectricity and electrical conductivity. However, piezoelectricity often requires electrical poling for activation. In this study, a candidate material containing thermoplastic polyurethane (TPU) and carbon black (CB) with conductive and flexible properties is incorporated with piezoelectric elements like polyvinylidene fluoride (PVDF) and barium titanate ($BaTiO_3$) to assess its suitability for sensor applications without electrical poling. Texturing the surface of $BaTiO_3$ particles and adding tetraphenylphosphonium chloride (TPPC) to the composite are evaluated as non-poling treatments to improve the sensor response. It was found that TPU and PVDF produced segregated domain structures within the printed sensors that aligned along the printing direction. Due to the effect of this preferential orientation combined with the presence of raster-raster interfaces, printed sensors exhibited significant electrical anisotropy registering greater electrical waveforms when the electrodes aligned parallel to the raster direction. An improvement of current baseline from 0.4 μA to 12 μA in the parallel direction was observed in sensors functionalised with both treatments. Similarly, when the waveform responses were measured under a standardised impact force, current amplitudes in both orientations registered a twofold increase for any impact force when both treatments were applied to the feedstock material. The results achieved within this study elucidate how composite formulations can enhance the sensor response prior to conducting electrical poling.

1. Introduction

Smart electronics with additional functionalities like flexibility and softness [1] have a crucial place in the advancement of Industry 4.0 and are a key enabling technology of the forthcoming Industry 5.0 digital era, where humans and machines combine [2]. Additive manufacturing, a.k.a. 3D printing, has a very important role within the development of smart electronics [3–5], combining rapid prototyping technology with custom designed materials specific for this application. One form of 3D printing in particular, Fused Filament Fabrication (FFF, a.k.a. fused deposition modeling, FDM, – belonging to the material extrusion category, MEX, according to ISO/ASTM 52900:2021), has been successfully utilized in the production of smart electronics such as triboelectric nanogenerators [6,7] and capacitive displacement sensors [8]. Sensors with soft and flexible properties are highly researched for biomedical applications [9], robotic devices such as artificial muscles [10] and wearable electronics [11]. FFF is ideally suited to assist with the growth of smart electronics by being able to deposit thermoplastic feedstock that can conduct electricity. Unlike traditional metallic conductors, FFF conductive composites can be soft, flexible and, importantly, resistant to corrosion owing to the appropriate choice of the polymer matrix [12–14].

Sensors imbued with conductive properties can be complemented with piezoelectric properties. To this aim, printing polymers are often modified with piezoelectric fillers like barium titanate [15], zinc oxide [16], lead zirconate titanate [17] or piezoelectric polymers such as the

* Corresponding author.
E-mail address: Dejana.pejak@csiro.au (D.P. Simunec).

https://doi.org/10.1016/j.addma.2023.103679
Received 17 December 2022; Received in revised form 30 April 2023; Accepted 27 June 2023
Available online 29 June 2023

co-polymers of polyvinylidene fluoride (PVDF) [18]. If 3D printing is conducted under room temperature, the functional filler can be dispersed and printed in a polymeric solution [19] which retains piezoelectric properties since the process occurs below the Curie temperature [20,21]. However, this printing process comes with some safety concerns including the potential toxicity of the rapidly evaporating solvent, especially if potentially harmful compounds like dimethylformaldehyde (DMF) are in use [22] Also, the severe constraints on part size and dimensional accuracy are technical limitations that hinder the industrial uptake of solution-based 3D printing. Conversely, larger and more accurate parts can be printed by FFF. Moreover, being solvent-free, FFF works in a safer and scalable manner. Nonetheless, since thermoplastic composite feedstocks in FFF are heated to a molten state, the processing temperature may easily exceed the Curie temperature of the piezoelectric additives, which will subsequently lose their piezoelectric properties, as these largely depend on the existence of spatially organised dielectric dipoles. To prevent the loss of the piezoelectric configuration, printed parts generally require to be polarized, which is typically achieved by electric field assisted FFF. In this method, an electric field is generated around the part as it is being printed to induce the alignment of the piezoelectric structures within the composite. This ordered structure is then "locked" into place upon cooling [23]. Though very effective, poling may require electrical fields in the order of 1 MV/m [24] because popular piezoelectric components like PVDF and barium titanate ($BaTiO_3$) themselves are not inherently conductive. Quite the opposite, they have a high electrical resistance (e.g., 2×10^{14} Ω/cm for PVDF [25]), and this drastically limits the effectiveness of external electric fields. As a consequence, while FFF may be ideal to implement electrical poling into the printing process, this does, however, pose a critical risk to the user, due to the potentially deadly high voltage in use (between 10 kV [26] and 12 kV [27]). Conceivably, electrical poling is not feasible with standard printers, and the hazard is incompatible with the widespread adoption of FFF for do-it yourself (DIY) and educational purposes, or for small industrial scale production and rapid prototyping. Moreover, in this experimental set-up the print bed and the nozzle act as the cathode and anode respectively. With additional layers of material being printed, print bed and nozzle move further away from one another, causing a progressive decrease in the electrical field which, if not properly counteracted, would likely result in a weaker piezoelectric response as a function of the part's growth. This makes the manufacture of bulky, non-planar objects with a piezoelectric response extremely challenging.

To avoid utilising high voltage, other methods exist to encourage self-poling of piezoelectric structures. This is still an emerging field of research, and very few examples of self-poling structures have been mentioned so far in the literature regarding melt extruded composites for FFF. Guo et al. [28] exploited the flow-induced crystallization of PVDF to encourage the alignment of piezoelectric β-phase crystals using microinjection as a novel printing strategy that produces high shear stresses. Dopamine-functionalized carbon nanotubes were also added to stabilise the crystal alignment. Pei et al. [29] encouraged the piezoelectric properties of PVDF with tetraphenylphosphonium chloride (TPPC), and this resulted in a composite being able to power five light-emitting diode (LED) lights without field-assisted poling. Subsequently, Pei et al. [30] improved this composite material by blending $BaTiO_3$ powder that had been mechanically activated through a novel milling process. Although the addition of mechanically activated $BaTiO_3$ ameliorated the piezoelectric properties of PVDF, polarization was still applied on the final printed part [30]. To the best of the authors' knowledge, thus far these are the only studies related to the production of FFF printable parts with self-poling mechanisms to encourage piezoelectricity in PVDF-based composites.

Another issue in the literature, piezoelectric charges are often collected using electrodes locally attached to the printed object [31] which may limit their implantation in soft robotic devices. If the material is not electrically conductive, charges can only be collected from the area touching the electrode, and this may underestimate the charges being generated within the part. In addition, it is unclear if the current being measured is a result of the entire sample or just the current registered in the region of the conductive wires. It is questionable whether surface or localised charges are measured, since the bulk contribution of piezoelectricity is not accessed because of volume effects. Conversely, if a conductive pathway is established within the composite, this can improve the delivery of current from the piezoelectric elements (like PVDF or $BaTiO_3$) and provide a method for reliably detecting piezoelectric output [32]. Noteworthy, the presence of a conductive pathway may also improve the transmission of current to the piezoelectric fillers, thus lowering the electric field required for poling. For example, incorporating a conductive element like polyaniline (PANI) into a PVDF/$BaTiO_3$ composite has been shown to reduce the voltage required to polarize PVDF and $BaTiO_3$ [33].

Another point to consider is that FFF printing with PVDF produces parts that are stiff and inflexible, and therefore unsuitable for applications like soft electronics. Accounting for these current limitations requires a paradigm shift leading to the development of a new composite with the desired properties such as ease of printing, high flexibility, softness, electrical conductivity, and piezoelectricity. In this way, the risky and cumbersome poling process can be sidestepped, and functional requirements can be met through the skilful formulation of composite materials.

Herein, we introduce and investigate a composite blend that is soft and flexible as well as conductive with piezoelectric constituent phases to evaluate the effectiveness of self-poling mechanisms like the addition of TPPC and the mechanical activation of $BaTiO_3$. The multi-material composite is comprised of piezoelectric elements (PVDF and $BaTiO_3$) that are blended with a conductive ingredient made of thermoplastic polyurethane (TPU) and carbon black (CB). 3D printed sensors are fabricated by FFF, and then investigated for their response waveforms to assess their sensor capability without any polarisation. The effect of adding TPPC and $BaTiO_3$, the latter either milled or unmilled, is investigated to understand the importance of these treatments on the sensor's output and their interaction with the composite matrix.

2. Materials and methods

2.1. Materials

For the conductive component of the composite, a TPU matrix filament was purchased as NinjaTek "EEL" filament (1.75 mm diameter, containing 18 wt% carbon black [34]) and pelletized into 5 mm lengths. For the piezoelectric components, PVDF pellets (Kynar 740) were donated by Arkema. $BaTiO_3$ powder (99.95% purity, 100 nm average particle diameter [35]) and TPPC (98% purity) were purchased from Inframat Advanced Materials and Sigma-Aldrich, respectively. Dried $BaTiO_3$ powder was milled by placing 50 g in a semi-continuous Rocklabs ring mill for 30 min using a tungsten carbide head. If not otherwise stated, all materials used in this study were dried overnight at 70 °C before use.

2.2. Manufacture of piezoelectric filaments

The piezoelectric component of the FFF filament was first obtained by mixing $BaTiO_3$, either unmilled or milled, with dried PVDF pellets in a PRISM Eurolab 16 twin-screw extruder (Fig. 1a). The heating zones were programmed as follows: 220, 210, 200, 180, 150, 110, 70, 20, 20 °C. The filament was extruded at a screw speed of 160 rpm through a 2 mm die, heated to 230 °C.

In order to produce TPPC-functionalised composites, PVDF-$BaTiO_3$ filaments were pelletised and re-extruded with an addition of 5 wt% of TPPC (Fig. 1b). Pelletized and dried portions of the PVDF/$BaTiO_3$ or PVDF/$BaTiO_3$/TPPC and TPU/CB (EEL) filaments were added to the hopper in a 50:50 (wt:wt) ratio and extruded again through the twin-

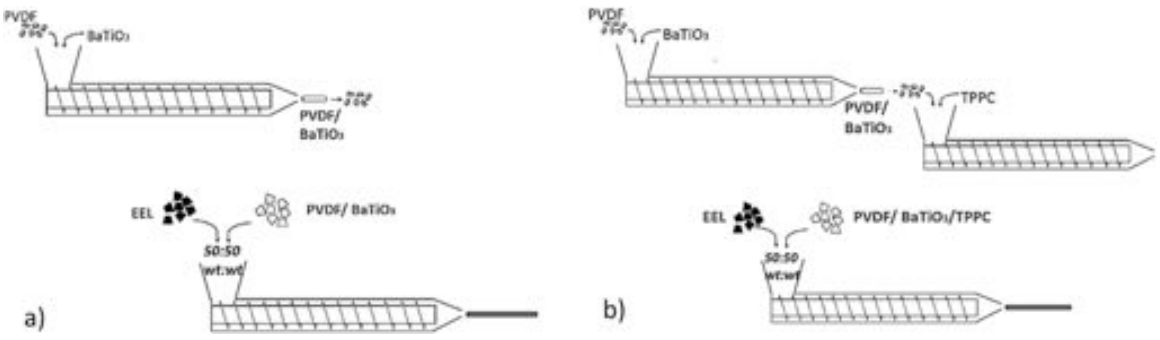

Fig. 1. Producing piezoelectric matrices and blending into TPU/CB (EEL) filament (a) without TPPC and(b) with TPPC.

screw extruder to obtain the TPU/CB (EEL)-functionalised composite filaments.

Due to the mixing occurring within the twin screw extruder and consequent uneven pressures, the extruded filaments did not have a stable diameter. Therefore, twin screw extrusion was followed by additional pelletization and extrusion with a single screw extruder (Filastruder) heated to 215 °C. This resulted in a consistent filament diameter ranging between 1.70 and 1.80 mm. The filaments fabricated in accordance with Table 1 should be homogenous and dark grey in colour. For the sake of brevity, filaments containing piezoelectric components will be named hereafter as "piezoelectric" or "P filaments", as opposed to the neat TPU/CB (EEL) filament (which is the electrically conductive ingredient). Four different P filaments were compared to evaluate the effectiveness of different treatments. All P filaments contain 50:50 (wt:wt) blend of TPU/CB (EEL) and PVDF/ $BaTiO_3$ (P1) with either the addition of TPPC (P2), milled $BaTiO_3$ instead of pristine $BaTiO_3$ (P3) and milled $BaTiO_3$ with an additional incorporation of TPPC (P4).

2.3. FFF printing and piezoelectric property testing

All sensors were produced using a Creality C-10 printer fitted with a 0.8 mm hardened steel nozzle. One layer thick (0.2 mm) square samples measuring 30 mm were printed at 230 °C, bed temperature of 100 °C and 10 mm/s print speed (Fig. 2). Neat TPU/CB (EEL) sensors were also printed for comparison purposes.

Since no standard procedure exists in the literature, a new custom-made testing apparatus is proposed here for the first time to enable the accurate assessment of the piezoelectric response of FFF sensors. Owing to its structural simplicity, ease of use, and reliability in testing AM parts, including flexible and strongly anisotropic ones, this new printed circuit board (PCB) design can become a practical tool for all researchers and developers working in the field.

The samples were mounted to a custom-made piezoelectric test rig (Fig. 3) comprised of a PCB board with a milled copper square on one side acting as an anode and with milled copper circuits on the other side acting as cathodes. The reason for having copper circuits (instead of a continuous copper plate) on one side is to examine any anisotropic effects that may be due to the alignment of the printed rasters. The test was thus repeated with the circuits being normal or parallel to the rasters, denoted as 90° and 0° test configurations, respectively. Since the contour of the printed sensors may interfere with this measurement, the squares were trimmed to a size of 25 mm. The circuits were connected via 2 mm banana clips to a BioLogic potentiostat equipped with a low current module. Full details are reported in Appendix A, Supplementary Information.

Cyclic voltammetry (CV) scans were conducted at 20 mV/s for 10 cycles at − 2.5–2.5 V to characterise the electrical performance of the sensors depending on their composite formulations (the effect of scan speed is discussed in Appendix B, Supplementary Information). Chronoamperometry (CA) scans were conducted using a 0.1 V probe voltage (Fig. 4). Two different types of chronoamperometry scans were conducted. In order to mimic the behaviour of the soft sensors as wearable smart devices, the first test used a simple finger pressing motion to determine the waveform responses (Fig. 4a). The second method used steel tubes (measuring 10, 20 and 30 cm in length) dropped from a constant height of 20 mm onto the PCB board to measure the waveform response under a standardised force (Fig. 4b). In both cases, the CA test was repeated after loading to identify any change mechanically induced in the sensor's response. Additional details are found in Appendix C, Supplementary Information.

Table 1
Table of piezoelectric FFF filaments.

Notation	50 wt% TPU/CB (EEL): 50 wt% PVDF/$BaTiO_3$ with
P1	Unmilled $BaTiO_3$, no TPPC
P2	Unmilled $BaTiO_3$ plus TPPC (5 wt%)
P3	Milled $BaTiO_3$, no TPPC
P4	Milled $BaTiO_3$ plus TPPC (5 wt%)

2.4. Materials characterisation

Fourier Transform InfraRed (FTIR) scans were conducted on the printed sensors with a Nicolet6700 FTIR. Four separate scans were collected in different areas of each printed sensor (P1 to P4).

A Rigaku SmartLab, equipped with a rotating anode CuKα source (45 kV, 200 mA) and Hypix 3000 detector, was employed to obtain the X-ray diffractograms. The diffractometer was operated in parallel beam mode with a 1 mm incidence slit, 20 mm receiving slit and a beam limiting mask of 10 mm. For all samples, data was collected over the 2θ range 5–90° with a step size of 0.04° and a scan rate of 2° per minute. Analyses were performed on the collected XRD data using the Bruker XRD search match program EVA™6. Crystalline phases were identified using the ICDD-JCPDS powder diffraction database. Rietveld analysis was performed on the data using the Bruker TOPAS™ V6 program to determine crystallite size. Background signal was described using a combination of Chebyshev polynomial linear interpolation function and 1/x function. Cell parameters, vertical sample displacement, peak full width at half maximum, and scale factor were all refined. For crystallite size, error ranges were calculated based on three estimated standard deviations as calculated by TOPAS.

For the differential scanning calorimetry (DSC), a Mettler Toledo DSC 3 system equipped with an intracooler was employed. A fragment of each sensor (sample weighing approximately 10 mg) was sealed in an aluminium crucible, which was first cooled to 0 °C and then heated to 300 °C all at 5 °C/min heating/cooling rate under nitrogen purge at 40 mL/min flow rate. The degree of crystallinity (X_c) of the composites was calculated in Eq. 1:

$$X_c = \frac{\left(\left(\Delta H_{f\beta} * \emptyset\right) + \left(\Delta H_{f\alpha} * (1 - \emptyset)\right) \bullet \Theta\right)}{\Delta H_f^*} \quad (1)$$

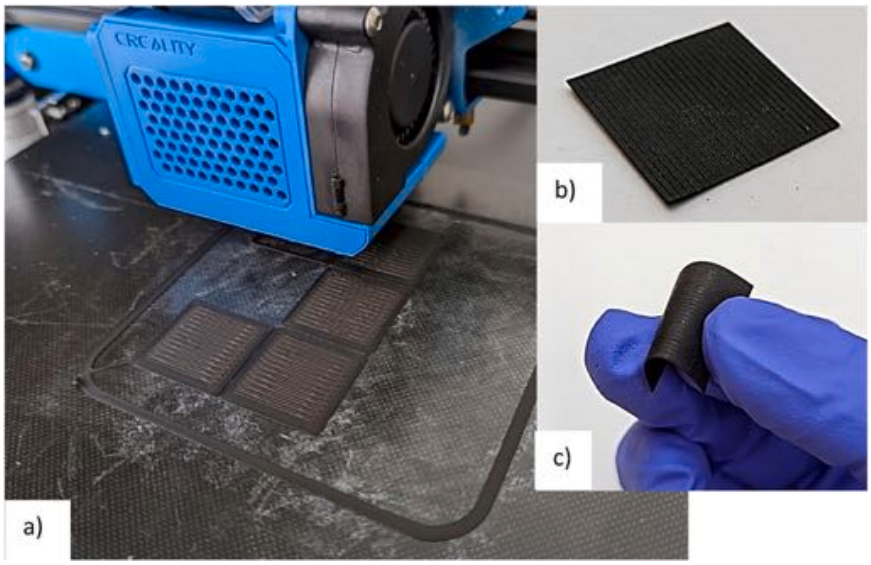

Fig. 2. a) Image of the printing process of the piezoelectric test samples; b) trimmed P1 sample and c) flexibility of the P1 sensor. All samples measure 30 mm as printed, and 25 mm after trimming.

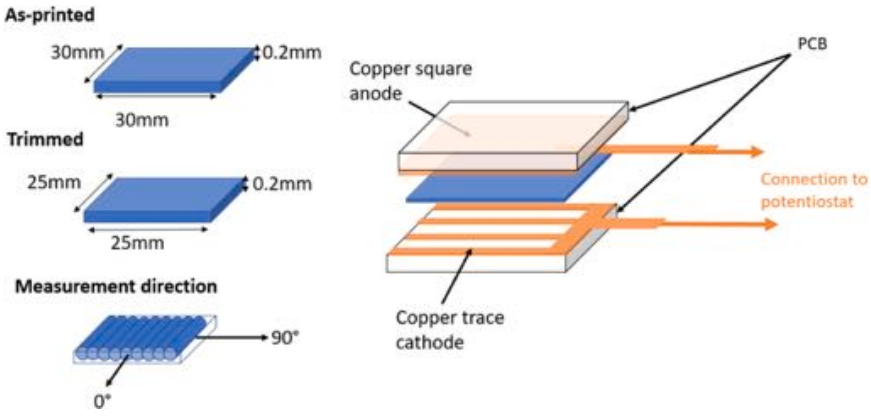

Fig. 3. Schematic drawing of the piezoelectric test rig and sensor's preparation for testing.

Where ϕ is the amount of β phase in PVDF estimated from the FTIR scans, and $\Delta H_{f\alpha}^*$ and $\Delta H_{f\beta}^*$ are the specific melting enthalpies of the α and β phases in 100% crystalline PVDF, corresponding to 104.5 and 103.4 J/g respectively [36]. ΔH_f is the melting enthalpy of the blends extracted from DSC curves and $\Theta = 0.5$ is the approximate weight fraction of PVDF in the printed sensors (P1, P2, P3 and P4).

The thermogravimetric analysis (TGA) of the samples was completed with a Mettler Toledo TGA 2 system. Samples were weighed in an alumina crucible and then heated to 600 °C at 10 °C/min under nitrogen purge at 40 mL/min flow rate.

Mounted samples on aluminium stubs were iridium coated to a thickness of 4 nm (50 mA for 30 s) using a Cressington 208HRD sputter coater to enable conduction to prevent charge accumulation in an electron microscope. The samples were imaged using a Zeiss Merlin FE-SEM (Field Emission Scanning Electron Microscope) operated in the secondary electron (SE) or in lens (IL) mode and back-scattered mode (BSE). BSE imaging enhances elemental contrast with low atomic elements appearing darker than higher atomic number elements. Energy dispersive spectroscopy (EDS) was used to identify elements present within the samples using the X-Max Extreme 100 mm2 windowless Silicon Drift Detector (SDD) detector from Oxford Instruments Pty Ltd. An accelerating voltage of 3–7 kV was used for imaging and 7 kV for EDS analysis.

The results are to be taken as semi-quantitative and only trends compared. The magnifications used are indicative of the scale bars shown in the images.

3. Results and discussion

3.1. CV curves

Fig. 5 shows the cyclic voltammetry scans increasing with each cycle (shown in black arrows) for each of the piezoelectric sensors. The response of the neat TPU/CB (EEL) sensor is also included as a term of comparison. The sensors all behave as resistor-type sensors (as also observed in other carbon resistor sensors [37]), where the neat TPU/CB (EEL) sensor is slightly non-linear, whereas the sensors blended with PVDF and $BaTiO_3$ are linear. However, most sensors obeying Ohms Law can be non-linear to an extent and the slight non-linearity is not considered significant [38]. All sensors also have an increasing hysteresis obeying Ohmic Law and showing an improvement in conductivity with repeated cycling from − 5–5 V DC at a rate of 20 mV/s. The highest current values peaking at over 100,000 μA were observed for the TPU/CB (EEL) sensor (Fig. 5a), which has an uninterrupted percolation pathway of carbon black particles, and thus has a lower electrical resistance than the sensors incorporating piezoelectric and additional binder materials. In particular, the CB pathway in the piezoelectric

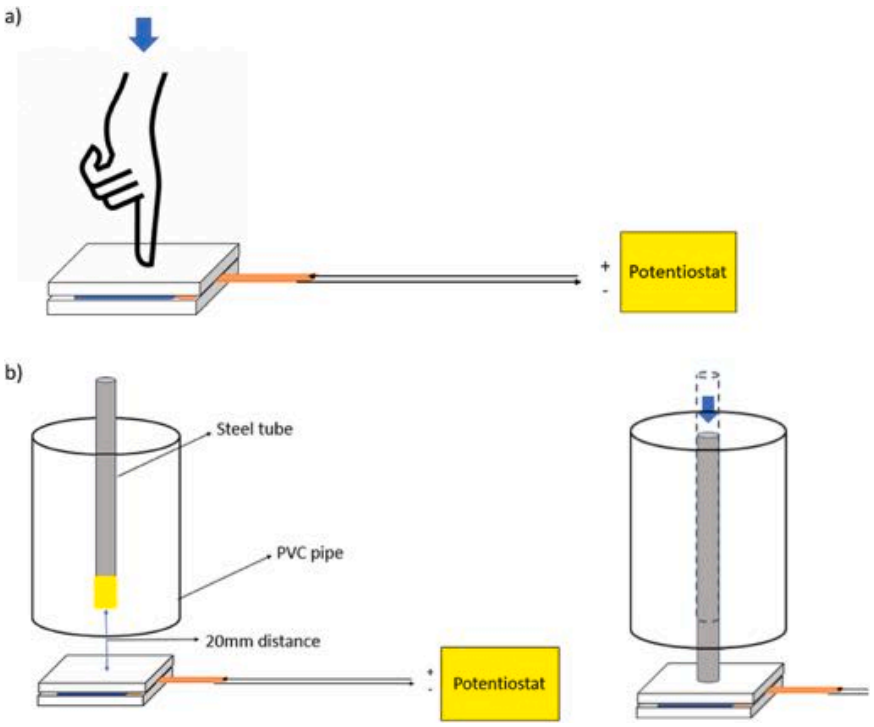

Fig. 4. Infographic for printed sensor chronoamperometry showing a) finger press test and b) constant force test (Additional information in Appendix C).

sensors became less continuous with the introduction of PVDF. As further discussed in Section 3.5.2, PVDF forms highly localised directional domains that are responsible for the increased electrical resistance of the P sensors over the neat TPU/CB (EEL).

For several reasons, the increasing hysteresis following each CV scan should be primarily attributed to the material interaction with the minor electric field generated during the CV scan itself. Firstly, given the linear nature of the cycles seen in each CV scan, it is unlikely that Joule heating is involved, since this would result in an increase in resistance and subsequent non-linearity, which was not observed in the CV scans. Secondly, no pressure was applied to the sensor during testing that could have affected the electrical contact between the copper traces and the sensor. Thirdly, all tested sensors were printed large enough to completely cover the copper traces, such that accidental contact between the copper traces is not possible.

The increase in hysteresis for each cycle appears to originate from the TPU/CB (EEL) matrix. Although the phenomenon is known from the literature, the exact reason for this increasing hysteresis in CB-based composites has not yet been fully elucidated. One prevailing theory is that the electrical resistance of CB composites is the sum of the electrical resistance of the CB aggregates and the resistance of the inter-aggregate space (i.e., the space that separates the aggregates, comprised of polymer which acts as an insulator) [39]. To cause a decrease in electrical resistance, either the aggregates or the inter-aggregate space must be changed in such a way that the percolation pathway is improved, and additional channels open up for electrons to flow as a parallel circuit. Since no evidence of melting or heating was observed during the scan, it is expected that the CB aggregates have not moved from their position as the polymer did not melt or heat enough to cause thermal expansion. It is therefore unlikely that the drop in the total electrical resistance observed within the sensors resulted directly from some reduction in resistance from the CB aggregates themselves. It is thus more probable that the resistance associated with the inter-aggregate space is being affected in some way. Since the inter-aggregate space is occupied by the polymer matrix, this space would have a very high electrical resistance due to the insulating nature of the polymer material. Reducing the distance between the CB aggregates or reducing the insulating effect between them (in the inter-aggregate space) would promote the establishment of parallel circuits within the matrix and thus lead to a decrease in electrical resistance. One example of this was reported in the study by Ji et al. [40], who found that the resistance of their carbon black/epoxy composite decreased due to electrical breakdown of the epoxy matrix within the inter-aggregate regions caused by the electrical field imposed upon the material during their current-voltage (I/V) characterisation (in this case specifically linear voltammetry scans, similar in nature to the CV scans reported in this study). The specific mechanisms of electrical breakdown of TPU are not well understood. However, as observed in the epoxy matrix investigated by Ji et al. [40], the electrical breakdown of TPU in the TPU/CB (EEL) material would reduce the resistance between the conductive CB particles. This would ultimately lead to the establishment of a parallel circuit, which has been observed in other CB studies [40–42]. The evolution of additional parallel circuits would explain the improvement in conductivity within all the sensors.

3.2. *Chronoamperometry – sensor orientation*

The effect of the sensor orientation is shown in Fig. 6 demonstrating that, for most cases, the current baseline within the chronoamperometry curves is higher when the infill of the printed sensor is aligned with the copper traces on the PCB board. P2, P3 and P4 demonstrated this behaviour, while for P1 the current baseline values did not differ significantly from one another (0.039 μA for 0°and 0.060 μA for 90°). The electrical anisotropic response shown here is consistent with the outcomes of other recent studies addressing electric properties in 3D printed structures [43] particularly for sheet-like sensors [44].

When comparing the current baseline variation between the two orientations (i.e., the current baseline at 0° direction vs. the current baseline at 90° direction) there is a significant degree of variation between the sensors. The TPU/CB (EEL) sensor showed a reduced anisotropic response compared with P2, P3 and P4 when the ratio of the two current baselines between 0° and 90° orientations is compared (1395 μA/795 μA= 1.75). This anisotropy likely originates from the raster-raster interfaces, which are known to interfere with the continuity of the conductive pathway of FFF composite parts [45]. However, other

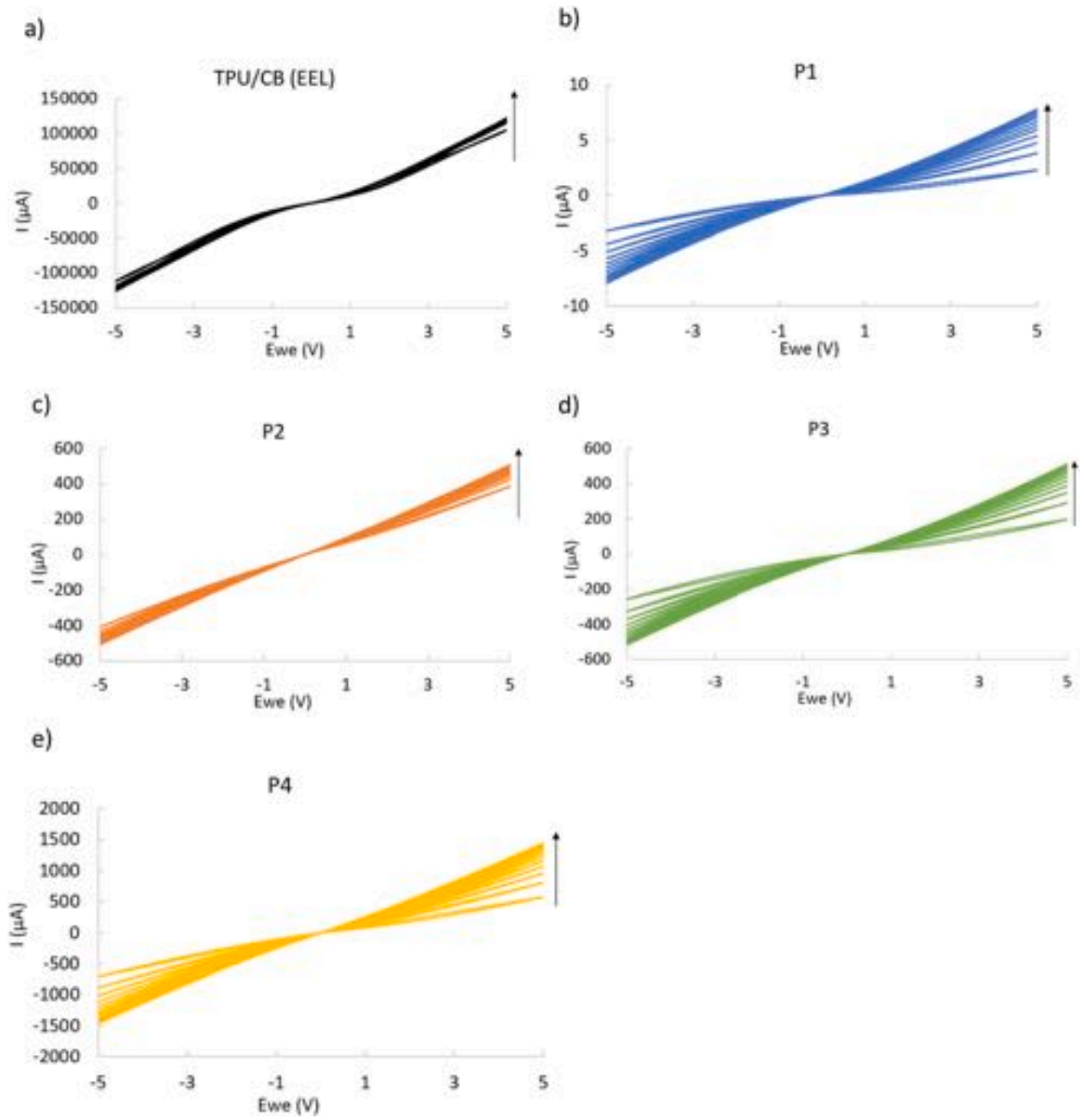

Fig. 5. CV scans for the printed sensors: a) TPU/CB (EEL), b) P1, c) P2, d) P3, e) P4, showing increasing hysteresis with the increase in scan number, as indicated by the direction of the black arrows.

microstructural features may be relevant, such as the aggregation of CB within the TPU matrix, combined with the shear forces in the printing process that would have aligned the CB agglomerates within the printing direction which has been verified in other FFF printed carbon black composites [46]. This effect is enhanced when combined with high viscosity and electrically insulating PVDF that is immiscible with TPU as demonstrated in Section 3.5.2. As compared to the neat TPU/CB (EEL) sensor, the current baseline ratios for the sensors blended with PVDF and $BaTiO_3$ had higher anisotropic responses, with the P2, P3 and P4 sensors featuring current baseline ratios of 1.84, 3.00 and 1.83, respectively. The strong anisotropic response observed for these sensors originated from their microstructure. As shown in the following sections, PVDF and TPU produce a segregated morphology, which aligns parallel to the print direction. This current baseline ratio for the P1 sensor was just 0.65. However, it should be mentioned that this value was likely affected by the very low signal response in P1, which may be difficult to discern against background noise.

3.3. Chronoamperometry – sensor composition

The chronoamperometric response for the sensors in the parallel orientation is shown in greater detail in Figs 7 and 8. The response of the piezoelectric sensors (Fig. 8) had to be graphed separately due to its high variation in current compared with the neat TPU/CB (EEL) sensor.

In contrast to the sawtooth-shaped spikes in current observed with the TPU/CB (EEL) material, the P sensors have a lower magnitude current response when pressed repeatedly, but still follow a similar pattern of spiking upwards every time force is manually applied. This reduction in intensity with respect to the neat TPU/CB (EEL) sensor is likely due to the disruption of the CB pathway within the TPU matrix caused by the multiple extrusion steps required to produce the P filaments. However, it is worth noting that there are substantial differences in the current spikes depending on the specific composition of the piezoelectric sensors. Fig. 8 demonstrates these stark differences, showing that the highest current waveforms were recorded in the P4 chronoamperometry, with values that were almost tenfold higher than those of the P1, P2 and P3 samples.

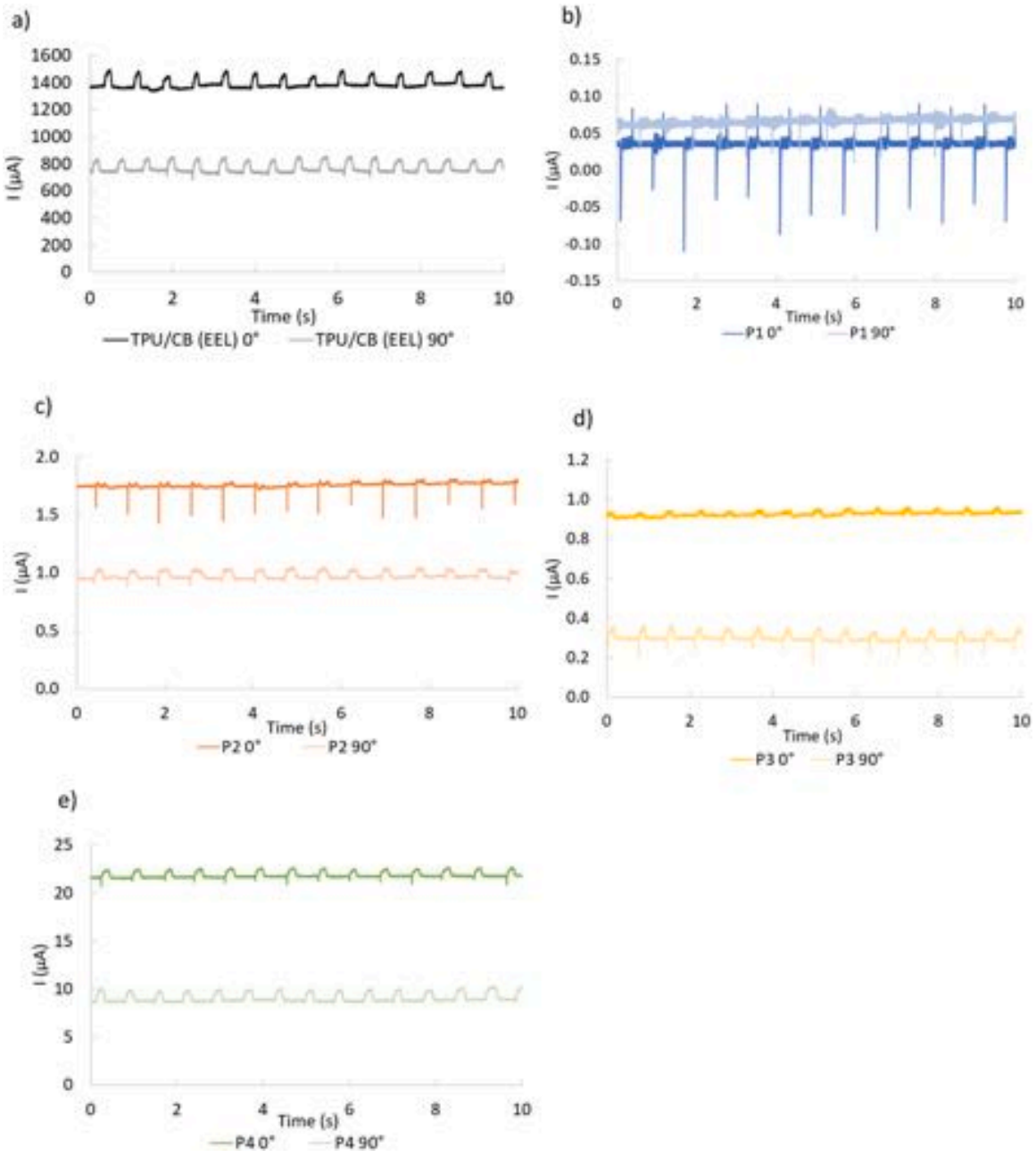

Fig. 6. Finger press tests in sensors first tested parallel (0°) and then rotated to be perpendicular (90°) to the copper traces for sensors a) TPU/CB (EEL), b) P1, c) P2, d) P3, e) P4.

The fact that no significant piezoelectric response is detected in any of the printed sensors confirms that the processing temperature is above the Curie temperature for all P composites and that the melt process itself cannot induce the correct piezoelectric configuration of $BaTiO_3$ and this grade of PVDF [47]. This effect was also observed in the study by Bodkhe et al. [48], where the melt extruded PVDF/$BaTiO_3$ composite did not exhibit any piezoelectric properties unless first electrically poled.

The piezoelectric filler $BaTiO_3$ is ferroelectric and generally requires electrical poling to become piezoelectric [48]. The piezoelectric polymer PVDF also requires to be in the β-phase to be piezoelectric. However, melt blending mainly produces the α-phase, which does not have piezoelectric properties [47]. The most common ways to transform these materials in their piezoelectric forms consist in conducting electrical poling [49], adding different fillers which increase the amount of the β-phase over the α-phase in PVDF [16,50,51], or thermally annealing $BaTiO_3$ at the Curie temperature [52]. On the other hand, the processing temperatures required for extruding and FFF printing exceed the Curie temperature of PVDF which can range between 180–195 °C and is dependent on PVDF co-monomer content [53] [54].

The lowest response in the CA curves came from the P1 sensor, indicating very small waveform spikes reaching 0.01 μA, and with significant noise being detected during the test. The addition of TPPC to the composite (in P2) resulted in an improved waveform response at a higher current of 1.74 μA. In other studies, TPPC was able to successfully improve the piezoelectricity of PVDF by increasing the presence of β-phase crystals by up to 85% [29]. This effect has also been reported for other quaternary phosphonium salts that, like TPPC, are able to promote the α-to-β phase transformation in PVDF even if added in small amount [51]. This is because TPPC is able to attract -fluorine moieties within the PVDF chain and thus help PVDF orientate into β phase configurations [29]. Conversely, milling $BaTiO_3$ led to limited improvement to the CA

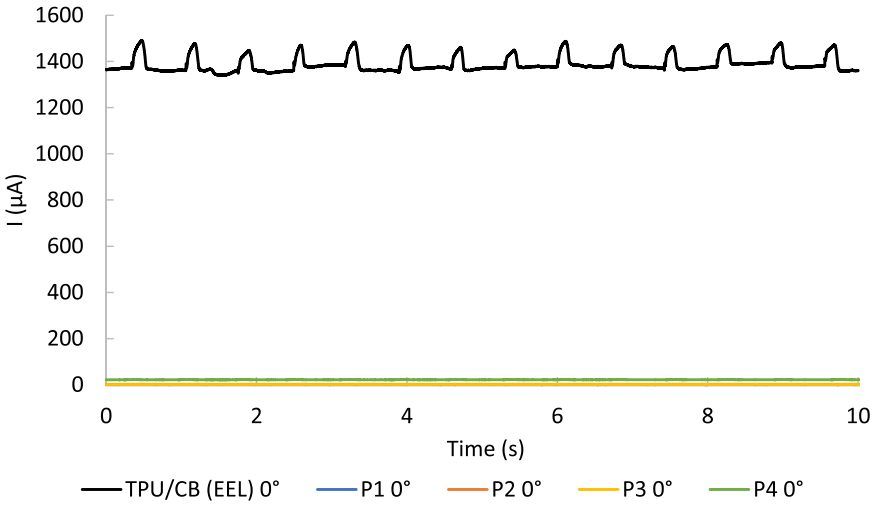

Fig. 7. Chronoamperometry scans for sensors in parallel direction.

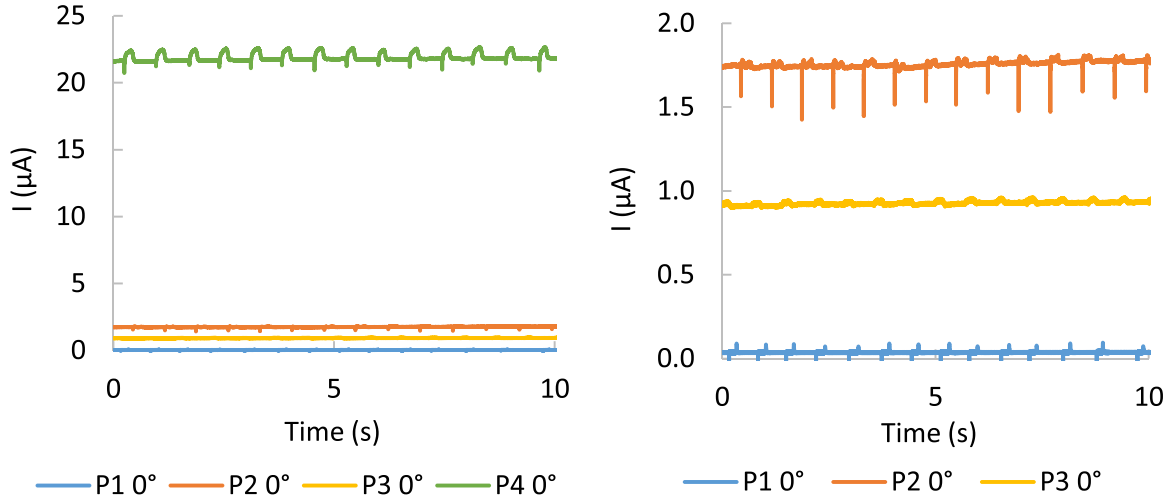

Fig. 8. Chronoamperometry scans for 0 ° direction a) showing all P sensors and b) close-up of scan for P1, P2 and P3 sensors.

scan, as P3 only had a slight improvement at 0.9 μA compared with P1 (containing pristine $BaTiO_3$). However, the highest electrical responses within the chronoamperometry scans of the sensors printed with the P filaments were observed in P4, which contained both milled $BaTiO_3$ and TPPC. Interestingly, milling $BaTiO_3$ effectively textured the surface of the particles with some size reduction (refer to Appendix D, Supporting Information). Although milled $BaTiO_3$ was present in both P3 and P4, only P4 benefitted from this treatment. This demonstrates that the crucial combination is adding TPPC and milled $BaTiO_3$ when extruding a filament for use in sensors' manufacture.

3.4. Chronoamperometry – current amplitude under standardised impact

Since the current baseline has been shown to shift upwards based on the CV curves (Fig. 5), it is better to compare the effect of sensor formulation and orientation by analysing the average change in current amplitude (Fig. 9) caused by the impact of the steel pipes. The averaging is done to account for any minor baseline drift since any major baseline drift would have been observed within the CV curves as a deviation from non-linearity.

The mean values of the current amplitudes taken from Figure C.2 in the Supplementary Information are displayed in Fig. 10. These were average values of at least 10 spikes with the margin of error to 95.0% confidence shown in the error bars.

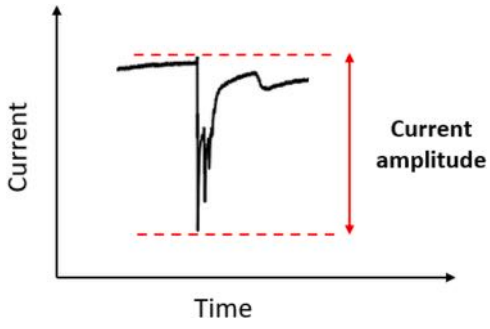

Fig. 9. Image showing where measurement of current amplitude was taken for each spike on the CA curves.

Fig. 10a shows that the highest amplitudes occurred in the TPU/CB (EEL) sensor due to its lower electrical resistance. Additionally, increasing the impact force heightened the current response. This trend was observed for both orientations. With the impact force being the same, the response at 0° direction was generally greater than that at 90° direction, except for the lowest impact load at 310mN. To improve the observation of the current amplitudes, P1 and P2 are plotted separately due to their significantly reduced amplitudes compared with the other

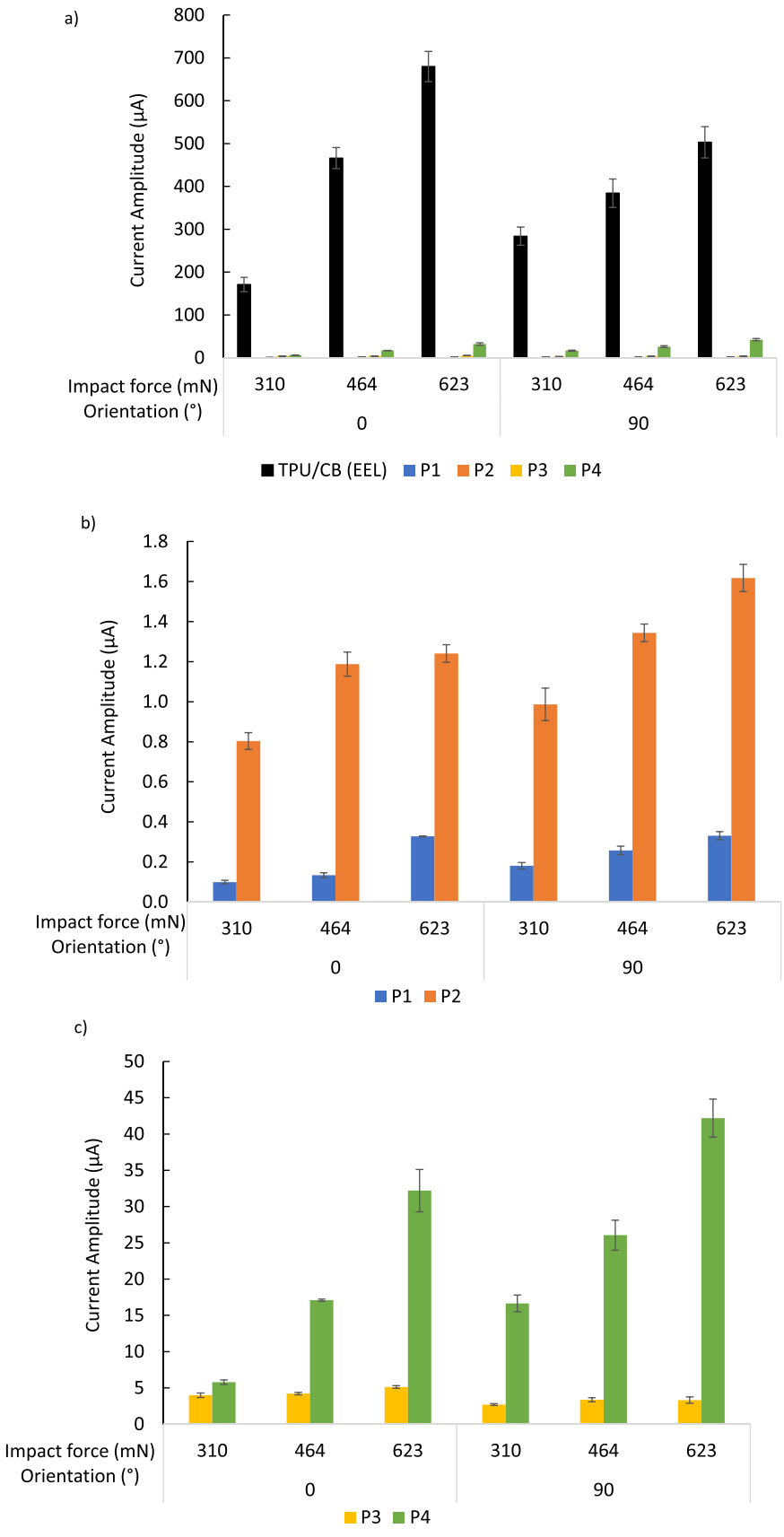

Fig. 10. Current amplitude (mean and error at 95% confidence) of the sensors in 0° and 90° orientations for all impact forces: a) showing all sensors, b) showing P1 and P2 only and c) showing P3 and P4 only.

sensors (Fig. 10b). As a general trend, P1 shows higher current amplitudes for the 90° direction than for the 0 ° direction. However, the scale of the current output recorded for this sensor (which ranges between 0.099 μA at minimum and 0.328 μA at maximum) is very low and hence possibly affected by noise, as the measurement is approaching the detection limit of the potentiometer in use. Compared to P1, the P2 sensor (with the incorporation of TPPC) displayed a nearly 10-fold increase in current amplitude, whereby the minimum average current amplitude was 0.80 μA (0° orientation, 310mN). In Fig. 10c, further improvement was registered for the P3 sensor, with another near 10-fold increase in current output (minimum average current amplitude value of 4.0 μA at 0° orientation and 310mN). Ultimately, the highest readings came from the P4 sensor, which incorporated both milled $BaTiO_3$ and TPPC (Fig. 10c).

Milling $BaTiO_3$ can promote its homogenous dispersion. The achievement of a uniform distribution of the conductive filler is crucial for producing efficient conductive polymer-matrix composites [45], and similar requirements also apply to piezoelectric composites [55]. Moreover, $BaTiO_3$ has negatively charged grain boundaries [56] that attract the positively charged sections of the PVDF chain with hydrogen moieties and thus favour crystallization of PVDF on the particles' surface [57]. Textured $BaTiO_3$ particles such as those produced after milling (as in P3 and P4) may have higher negative surface charges due to the uneven distribution of domain boundaries caused by texturing the surface and the generation of secondary satellite particles. The combination of charge attraction between TPPC (attracting negatively charged fluorine moieties) [29] and milled $BaTiO_3$ (attracting positively charged hydrogen moieties) [56] in P4 may be the reason for the relatively higher electrical response, as these factors acted synergistically to improve the dispersion of elements within the sensor and prevent significant disruption of the carbon black percolation network.

It is important to note that, unlike the finger press tests, with the standardised load configuration higher current amplitudes sometimes occurred when the sensor was orientated at 90°. This is particularly evident in the P2 and P4 samples that recorded higher current amplitudes when oriented at 90° at every impact force. This discrepancy may be due to the different loading rate and hence to the different structure of the waveforms recorded during the impact tests and the finger press tests. The sudden application of pressure occurring in the impact tests (refer to Supporting Information, Figure C.2) produced a sudden spike at the beginning of each waveform. This spike was absent in the finger press test, which provided a much more gradual application of pressure. At present, it is still unclear why this behaviour is occurring, and this certainly warrants further investigation in future. However, this is a useful indication to demonstrate the sensor's capability of detecting the sensor's response to both sudden and gradual loads, as commonly observed for wearable sensors [58].

Although PVDF and $BaTiO_3$ in the printed sensors are not in their optimal configuration for piezoelectricity, there appears to be some mechanism that effectively improves the ability of the composite to carry an electrical current as a consequence of the self-poling treatments. This is consistent with the observation that the electrical field required for electrical poling of piezoelectric components is reduced in the presence of conductive elements [33]. Therefore, the printed and unpoled sensors in the present study have the potential for being poled under significantly lower voltages than those customarily used to polarise piezoelectric sensors [59]. This will be explored further in future work.

3.5. SEM and EDS

3.5.1. Distribution of $BaTiO_3$ and carbon black

Fig. 11 shows the micrographs of the printed sensors with the corresponding EDS maps representing the distribution of titanium (Ti), barium (Ba), carbon (C) and oxygen (O). $BaTiO_3$ (through Ti and Ba) appears to be uniformly dispersed within the whole polymer matrix, which suggests some particles have migrated out of PVDF. This is a common feature for all filaments presented in this research. This migration can be ascribed to the multiple extrusion processes required to produce the filaments with piezoelectric components. It is unclear if the same redistribution into PVDF has occurred for CB as carbon itself is present in both TPU and CB, and therefore impossible to isolate. In addition, there are black voids within the EDS images that correspond to the existence of fluorine from the fluorine moieties within PVDF.

3.5.2. Distribution of PVDF

Fig. 12 shows the EDS results highlighting the distribution of PVDF (containing fluorine) within the piezoelectric printed sensors as a segregated structure which has also been observed in other studies since the polymers form an immisble blend [60]. Adding TPPC to the composite is shown to affect P2 and P4 in the same way, by reducing the agglomeration of PVDF. Whilst P1 has very large PVDF agglomerates, elongated and preferentially orientated in a direction as dictacted by the 3D printing process, P2 shows discontinous rounded structures measuring approximately 1–2 μm, and P3 and P4 are a mixture of elongated agglomerates/rounded structures. These are electrically non-conductive micro-domains, some of which are aligned and would impart a degree of electrical anisotropy to the printed object. Also, P3 and P4 appear to have finer dispersion of fluorine-rich areas which may be the result of the attraction between negatively charged $BaTiO_3$ and the hydrogen moiety portion of the PVDF chain. These surface charges are also amplified depending on how the $BaTiO_3$ is textured. Since smaller $BaTiO_3$ particles can distribute more evenly throughout the sensor matrix, they may also be able to attract the PVDF chains more effectively and coat them in a sort of shell-core structure, although this requires further investigation to be verified.

3.6. FTIR

Fig. 13 shows the FTIR spectra of the printed sensors, with TPU/CB (EEL) being included for reference. The presence of CB in the composite matrix results in extensive absorption under distinctive peaks that can also be observed for all the P sensors. The spectra related to CB published in the study by Zhang et al.[61] featured similar peaks at 1730 and 1699 cm^{-1}, which correspond to bonded C═O and free C═O bonding between CB and TPU. In addition, peaks corresponding to the presence of hydrogen bonding between CB and TPU, specifically at 1730, 1699 and 1411 cm^{-1}, can be detected in the spectra of both the P sensors and the TPU/CB (EEL) reference [61].

Fig. 14 shows the region of interest in the range between 700 and 1300 cm^{-1}. The peaks within this region more strongly correspond to the crystalline phases in PVDF, showing the presence of both α and β phase crystals. Using the intensity of the (unshifted) absorption peaks at 840 cm^{-1} (A_β) and 762 cm^{-1} (A_α) (corresponding to β and α crystalline phases respectively), the relative fraction of β phase ($f(\beta)$) in the printed samples is calculated using Eq. 2 [62,63]:

$$f(\beta) = \frac{X_\beta}{X_\alpha + X_\beta} \times 100 = \frac{A_\beta}{A_\beta + 1.26A_\alpha} \times 100 \quad (2)$$

where X_α and X_β are the mass fractions of the α and β crystalline phases. Table 2 shows the results calculated from Eq. 2. Similar values of $f(\beta)$ were observed following melt extrusion of PVDF in the study by Zhang et al. [64].

The P1 sensor has the highest level of thermally stable α phase crystals generally associated with melt extrusion of PVDF [65], whereas the desired β phase crystals are favoured in a temperature window between 5 and 90 °C, which is suitable for solution-based processing [66]. Interestingly, the addition of TPPC (P2 and P4) promotes a noticeable reduction in the α phase peaks (762, 794, 974 and 1180 cm^{-1}), and a substantial growth of the peaks at 840 (rocking and bending vibrations of hydrogen and fluorine moieties within the PVDF chain [66]) and

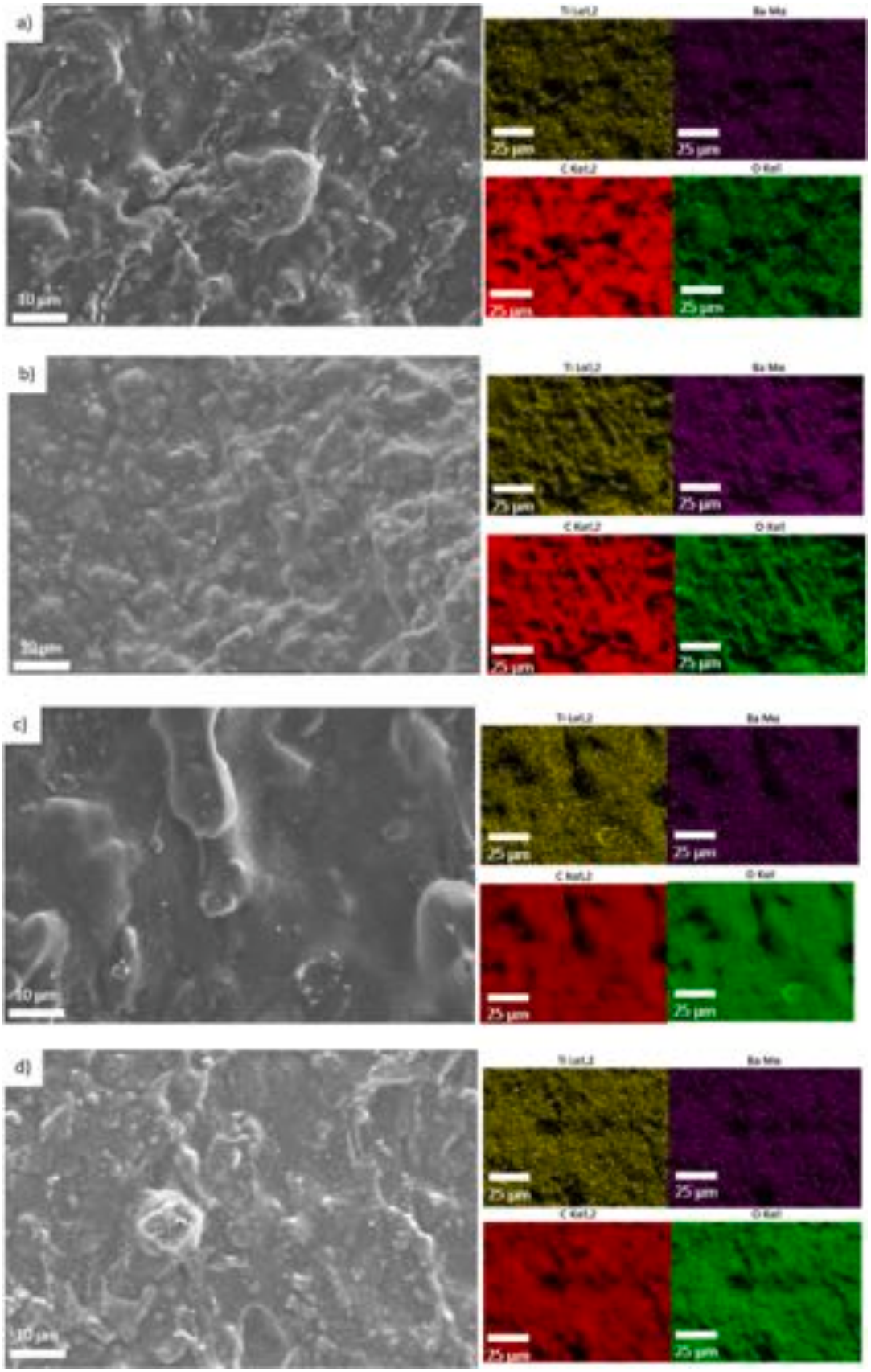

Fig. 11. SEM micrographs and corresponding EDS scans showing titanium, barium, carbon and oxygen distribution for a) P1, b) P2, c) P3 and d) P4.

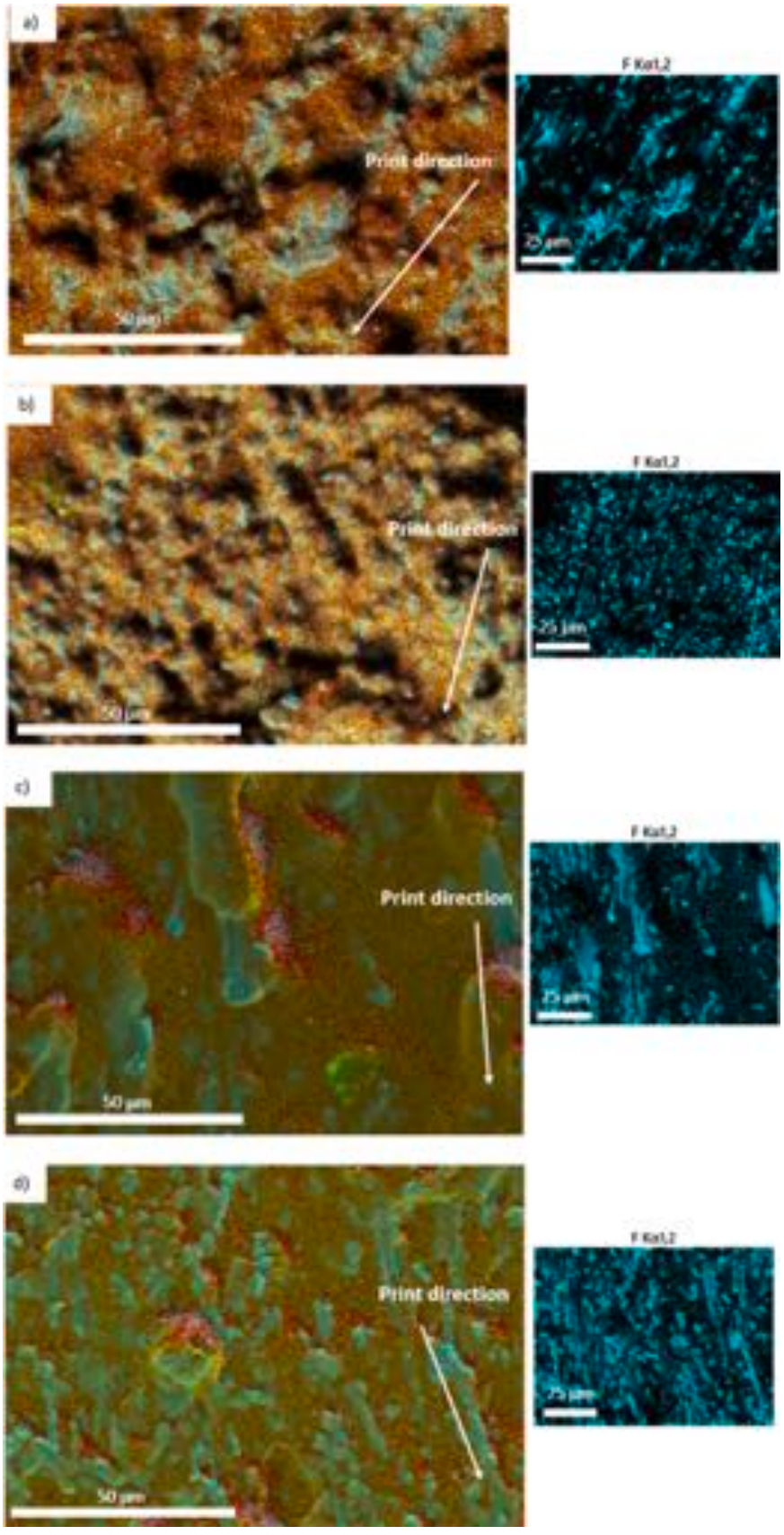

Fig. 12. EDS scans showing PVDF distribution and print direction for a) P1, b) P2, c) P3 and d) P4.

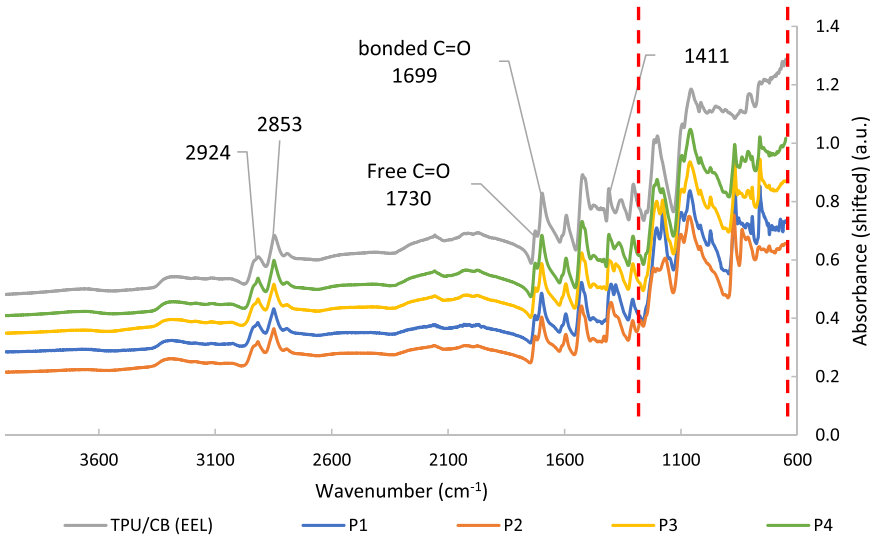

Fig. 13. Overlay of the FTIR spectra highlighting the region of interest (ROI) examined in Fig. 14.

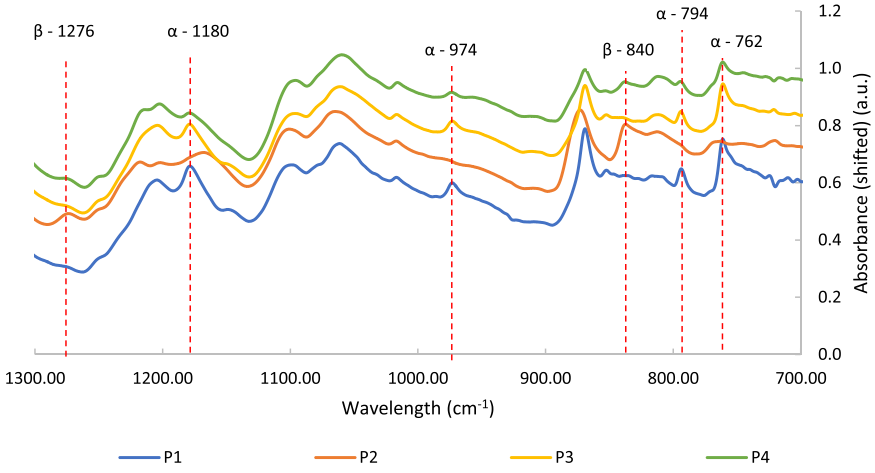

Fig. 14. FTIR spectra in the range 700–1300 cm^{-1}.

Table 2
Fraction (expressed as percentage with standard deviation) of β phase calculated from FTIR using 840 cm^{-1} (A_β) and 762 cm^{-1} (A_α) absorption peaks.

	Sample			
	P1	P2	P3	P4
$f(\beta)$ [%]	40.3 ± 0.40	46.1 ± 0.41	40.9 ± 0.21	42.8 ± 0.29

1276 cm^{-1}, which are characteristic bands of the β phase crystals [47]. While the absorbance at 840 cm^{-1} may also correspond to the γ phase in PVDF, the absence of the additional peak at 833 cm^{-1} confirms the crystallization of the β phase [65]. This effect is also observed in P3 and P4, although the reduced peak intensities may indicate a smaller proportion of crystalline structures (which was observed within the crystallinity levels in Table 4). Normally, $BaTiO_3$ effectively acts as a nucleation agent for PVDF, and smaller particles (such as those in P3 and P4) have been shown to promote β phase crystallization in PVDF in solution-based processes [67]. However, as demonstrated by the SEM/EDS analysis in Fig. 11, the smaller $BaTiO_3$ particles have partly migrated out of the PVDF matrix into TPU, and this may have reduced the availability of $BaTiO_3$ for nucleating the crystallisation of PVDF (in either polymorph) in P3 and P4. A smaller amount of $BaTiO_3$ within PVDF would result in fewer crystals being formed. Conversely, larger $BaTiO_3$ particles, as present in P1 and P2, would be more difficult to migrate out of the PVDF matrix. In P2, the transformation of α- to β-phase was evident in the FTIR scans that registered a 5% increase in β-phase crystals compared to P1. The increased presence of the piezoelectric β-phase in the P2 sensor was sufficient to improve its response waveform compared to P1 as already seen in Fig. 8b.

3.7. XRD

The diffractograms of the printed sensors are shown in Fig. 15. Both P1 and P3 clearly contain the α polymorph of PVDF (PDF 00–061-1403) with peaks in the spectra corresponding to the α crystalline planes (020), (110) and (021) [47]. In contrast, the intensity of the peaks is reduced or even negligible in the spectra of P2 and P4, which is consistent with the reduction of the α phase (i.e., increase of the β phase fraction) already detected through the FTIR scans. This indicates that the addition of TPPC inhibits the crystallization of the α-phase. In the XRD scans of P1, there is no detectable peak corresponding to the β-phase crystals of PVDF (PDF 00–061–1404), which should appear at 20.8° [68]. However, this may be due to the known difficulty of isolating the β phase in XRD spectra. As a matter of fact, in XRD spectra the α and β phases overlap with one another at the (110) reflection [47]. For this reason,

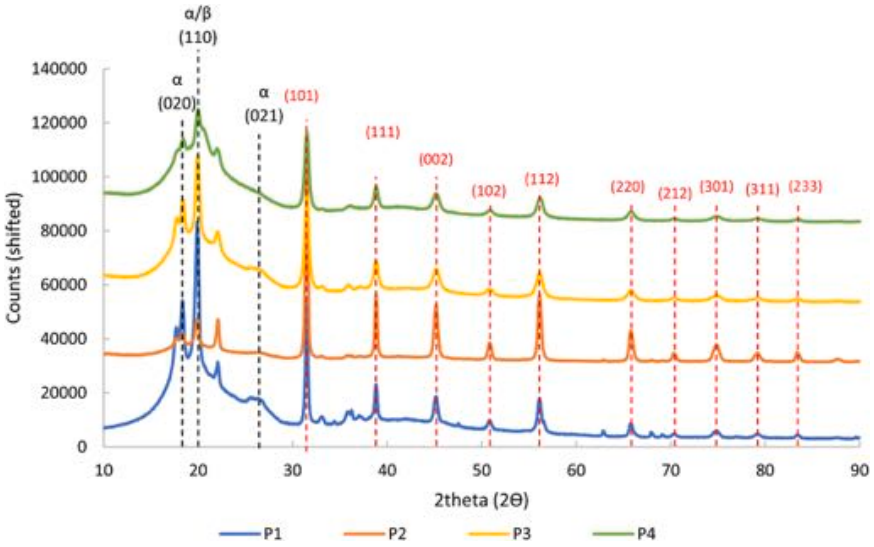

Fig. 15. XRD scans of printed sensors. Peaks corresponding to PVDF highlighted in black, peaks corresponding to $BaTiO_3$ highlighted in red.

FTIR and XRD scans are often used in conjunction in the literature for the detailed characterisation of PVDF samples.

The crystallite size of the distinctive α and β phases detected in the XRD scans is shown in Table 3. Adding TPPC effectively reduced the size of the α phase crystallites in the PVDF matrix as seen in P2 as compared to P1 and in P4 as compared to P3. The high error values in the calculation of the crystallite size of the β-phase are the result of the interference between the TPU peaks (two peaks from TPU at $2\theta = \sim 20°$ and $\sim 40°$) and the β phase peaks.

The analysis of the XRD spectra also confirmed the presence of the thermally stable cubic polymorph of $BaTiO_3$ (PDF 04–013–0298) in all samples including P3 and P4, which contained milled $BaTiO_3$ powder. None of the diffractograms exhibited the characteristic peak splitting at $2\Theta = 44–46°$, which is typical of the tetragonal structure [69]. The cubic configuration in $BaTiO_3$ is not piezoelectric and is generally associated with melt processing routes [70] like filament extrusion and FFF printing. The milling process resulted in reduced peak intensity amongst P3 and P4 sensors associated with a reduction of the cubic $BaTiO_3$ crystallite size (refer to Appendix E).

As for the potential nucleating effect of $BaTiO_3$, it has been reported that $BaTiO_3$ can enhance the β-phase crystallinity in PVDF in inkjet printing [71], but not in compression moulding [72]. González-Benito et al. [72] argued that the reason for the different polymorphism (or even its absence) in the PVDF samples is due to the variation in processing techniques. $BaTiO_3$/ PVDF composites produced by melt processing methods do not show any α- to β-phase transformation unless they are stretched heavily, which can occur in melt electrospinning [73]. Quite often, the β-phase can only be induced after poling [68]. This is consistent with the results of the XRD scan of the P1 sensor which did not show any trace of the β phase after 3D printing.

3.8. TGA

Fig. 16 shows the TGA results of the printed sensors. The TPU/CB (EEL) sensor shows a two-step degradation, with the first step beginning at 383 °C due to the cleavage of urethane bonds, and the second step at 430 °C due to the degradation of soft segments of TPU [74,75]. $BaTiO_3$ is stable on the whole temperature range under exam, with a slight decrease in mass by 0.2 wt% likely due to the removal of residual atmospheric moisture. Plain PVDF filament (also tested as a term of comparison) experienced extensive degradation at 470 °C with a residue of 31.2% due to char, resulting from polymer backbone unsaturation, caused by dehydrofluorination at the onset of degradation [76]. P1 has various degradation steps at onset temperatures of about 332, 337 and 538 °C. P3 (with milled $BaTiO_3$ instead of pristine $BaTiO_3$) has also three degradation temperatures at about 332 (identical to P1), 424 (higher than P1) and 463 °C (lower than P1). These three degradation temperatures likely correspond to the two degradation points already discussed in TPU/CB (EEL) followed by dehydrofluorination in PVDF responsible for the third degradation step. Interestingly, P2 and P4 sensors only have two degradation steps, with the first step occurring at 315 °C and the second step occurring over a broad range of temperature between 360 and 400 °C for P2, and between 349 and 401 °C for P4. It appears that the addition of TPPC in either P2 (unmilled $BaTiO_3$) or P4 (milled $BaTiO_3$) results in earlier degradation of the hard and soft segments in TPU (more significantly in P2 than in P4), although it is unclear why TPPC would have this effect on the composite. While additional tests would be required to understand the role of TPPC in the decomposition of TPU, all the degradation temperatures of the printed sensors largely exceed 300 °C, and this makes the developed composites suitable for FFF printing, provided that the maximum extrusion and printing temperature is in the order of 230 °C.

According to the manufacturer of the TPU/CB (EEL) filament, the material contains 18 wt% of CB [34], which is close to the value obtained from the scans here (21 wt%). Fluctuations and minor differences may be attributed to industrial scale production of the filament that may easily result in some local fluctuations of the filler fraction. There is also a slight variation in the amount of residue for the piezoelectric materials, with values of 30 wt% for P1, 36 wt% for P2, and 34 wt% for both P3 and P4. While it is difficult to verify exactly what the constituents of this residue are as it has already been confirmed that PVDF chars significantly due to dehydrofluorination, this identification falls outside the scope of this paper.

Table 3
Average crystallite size of the phases observed in the diffractograms of the P sensors.

Sample	α-PVDF (nm)	β-PVDF (nm)	BaTiO3 (nm)
P1	22 ± 1	Not detected	64 ± 3
P2	6 ± 2	20 ± 10	71 ± 9
P3	28 ± 4	20 ± 20	45 ± 9
P4	22 ± 5	20 ± 10	45 ± 9

3.9. DSC

The graphs in Fig. 17 report the DSC scans taken directly from the

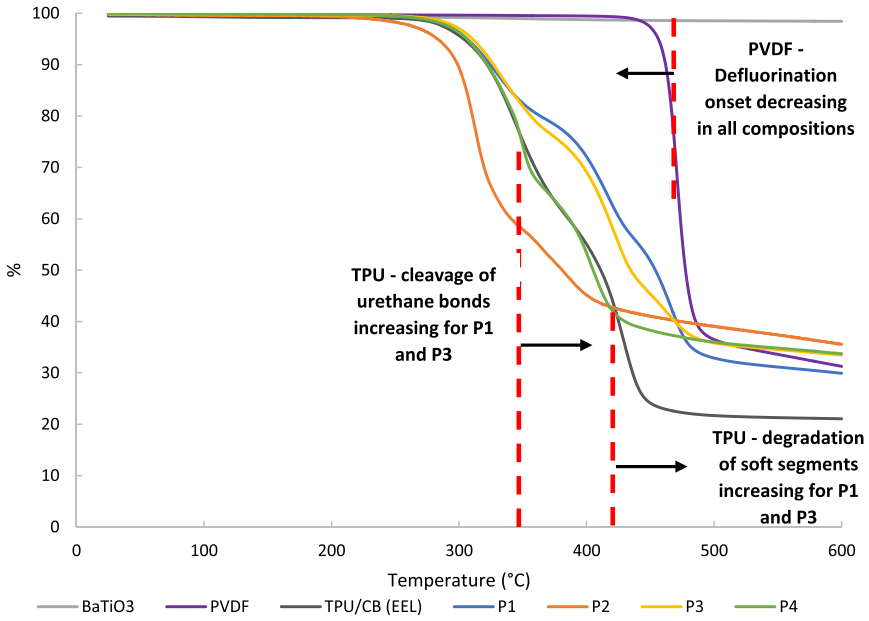

Fig. 16. TGA curves of the printed sensors over the 0–600 °C temperature range. $BaTiO_3$ and PVDF were also tested as terms of comparison.

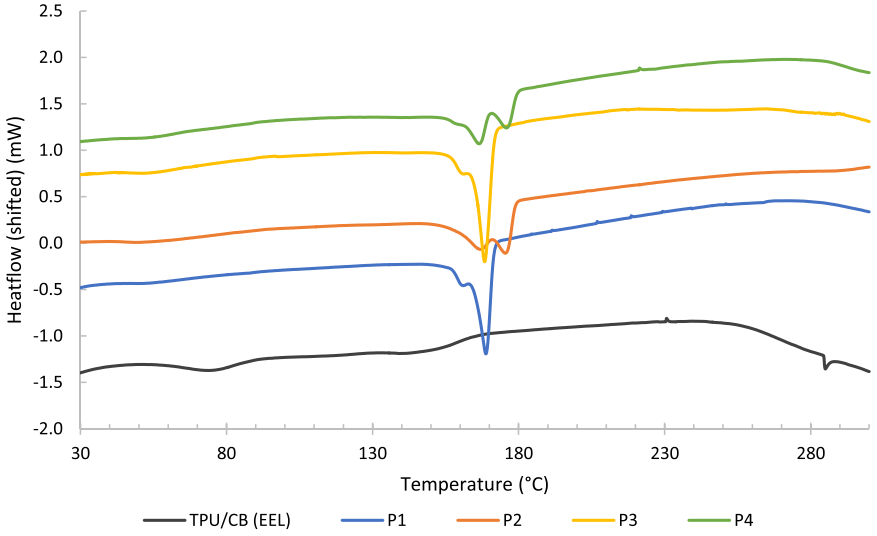

Fig. 17. DSC first heating curves for all printed sensors (exotherm down).

printed samples. In comparison to the TPU/CB (EEL) sensors, those printed with piezoelectric components (P1-P4) show a significant increase in crystallinity and appear to have multiple melting temperatures corresponding to various crystalline structures. The scan of the TPU/CB (EEL) sensor has two broad peaks at 74.7 and 148.1 °C, corresponding to the melting temperatures of the soft and hard segments of TPU [77]. These values do not reappear when TPU/CB (EEL) is combined with PVDF and $BaTiO_3$, as they are replaced by several melting peaks dependent on the sensor's composition (listed in Table 4). The shape of the P1 and P3 peaks matches the analysis of the α phase PVDF films published by Wallner et al. [78], which also exhibit a similar double melting peak. The shifting of the lower melting peak could be the result of the thickening in the lamellar (α crystalline structure) regions [78]. Conversely, the shape of the peaks is different for the composites combined with TPPC (i.e., P2 and P4), since it appears broader as typically reported for the melting peaks of the β phase of crystalline PVDF [47]. This confirms the FTIR results in Section 3.6 that adding TPPC favours the formation of the β phase. In addition, the shift of the melting peaks to higher temperatures, as well as the separation of the two endotherms, can be correlated with the effect of TPPC that results in a lower crystallization rate in PVDF [79].

Table 4
First (T_{m1}) and second melting temperatures (T_{m2}), normalized melting enthalpy (ΔH_f) and degree of crystallinity (X_C) extracted from DSC curves (Fig. 13).

Sample	Tm (°C)		ΔH_f (J/g)	X_C (%)
	Tm_1	Tm_2		
P1	160.4	169.1	15.75	7.5
P2	166.7	174.2	23.42	11.2
P3	160.5	168.3	12.17	5.8
P4	166.8	175.7	11.87	5.7

Table 4 summarises the data extracted from the DSC curves in Fig. 17. Each P sensor has at least two melting temperatures which may correspond to different PVDF crystalline phases. The exact determination of these crystalline phases in PVDF, however, cannot be conducted directly from DSC curves, as the α- and β-phases tend to overlap in the

range of 167–172 °C for pristine PVDF [47]. While the DSC scans show that the melting temperatures are in the 160–176 °C range for all materials, preliminary trials demonstrated that the printing temperature had to be raised to 230 °C in order to achieve a consistent flow through the print nozzle. Changing the printing temperature by increasing it further above 230 °C would likely favour the preferential alignment of the PVDF domains due to the lower melt viscosity. However, increasing the printing temperature would likely have a very limited effect on the piezoelectric components, as they would similarly become disoriented after printing.

Between P1 and P2, the addition of TPPC increased the crystallinity of the sample by 3.7%, which is in contrast with the results reported by Pei et al. [29], who found that TPPC effectively decreases the crystallization rate (and thus the crystallinity fraction) of PVDF and attributed this effect to the bulkiness of the TPPC molecules (containing four benzene rings). However, this difference may be due to the different grade of the polymers in use. Injection-grade PVDF such as the one used in the study by Pei et al. [29] is likely to have short polymer chains. Low molecular weight PVDF is more likely to have an unfolded configuration [80]. The addition of the bulky TPPC molecules would thus hinder the crystallization of PVDF. Conversely, in the present investigation a high molecular weight PVDF (with longer polymeric chains) was specifically chosen to withstand repeated thermal processing as required for producing and printing the filaments. On the one hand, due to these multiple extrusions required to fabricate the sensors, long PVDF chains would be heavily aligned and would not have the same polymeric configurations as other studies with less thermal processing. On the other hand, in spite of the processing-induced alignment, longer PVDF chains would be unable to promptly fold into crystalline configurations [80] and, in principle, would benefit greatly from the addition of TPPC as nucleating agent.

The addition of milled $BaTiO_3$ had interesting effects on the crystallinity of the composites, with the crystallinity of P3 and P4 being on average lower than that of P1 and P2. In the literature, milling-induced mechanical activation of $BaTiO_3$ was shown to increase the crystallinity of PVDF [81,82]. In room temperature manufacturing methods like solution casting, this increase in crystallinity is usually associated with the growth of the β-phase configuration [70]. In the present contribution, the relatively low crystallisation observed in P3 and P4 may be attributed to the partial movement of the finer (milled) $BaTiO_3$ particles out of the PVDF matrix into the TPU matrix, as already observed in the EDS images (Fig. 10c and d). This may be partly due to the reduction in size of $BaTiO_3$ nanoparticles, which can distribute more effectively within the TPU/PVDF matrix and thus may be less likely to be localised within PVDF resulting in lower crystallinity.

This migration of smaller $BaTiO_3$ particles may explain the higher crystallinity in P1 compared with P3, and P2 compared with P4. However, the surprisingly low crystallinity of P4 as compared to P2 should be scrutinised further, also taking into consideration that P4 contained TPPC. While TPPC proved to be an effective nucleating agent for PVDF in P2, the same did not happen in P4, and this may be indicative of competitive surface charge effects. Since PVDF in this study undergoes melt extrusion and hence prevalently crystallises in the α-phase, the spatial arrangement of the fluorine and hydrogen moieties within the PVDF chains causes them to be in close proximity to one another (whereas in the β-phase these side groups are neatly separated on either side of the carbon backbone). As a result, the neat charge associated with α phase is relatively low, with the fluorine moiety section of the PVDF chain being negatively charged and the side with the hydrogen moiety being positively charged. Consequently, the mechanically activated (milled) and strongly negatively charged $BaTiO_3$ particles may preferentially attract positively charged TPPC nanoparticles instead of PVDF, which would explain the lower crystallinity levels in P4 compared with P2.

4. Conclusions

Sensors were printed by fused filament fabrication (material extrusion additive manufacturing) with various composite filaments specifically formulated to the aim of reducing the need for poling. The microstructure and electrical response of the sensors were characterised to determine the impact that material composition and processing had on sensor performance. Four different formulations were prepared, all using a 50:50 wt% blend of conductive thermoplastic polyurethane/carbon black (TPU/CB (EEL)) matrix and piezoelectric polyvinylidene fluoride/barium titanate (PVDF/$BaTiO_3$) component. P1 sensors incorporated pristine $BaTiO_3$ powder, P2 utilised the same $BaTiO_3$ powder with an addition of 5 wt% TPPC. P3 and P4 used milled $BaTiO_3$ powder instead of pristine powder with P4 having the same addition of 5 wt% TPPC. All materials blended with the PVDF/$BaTiO_3$ piezoelectric component showed a reduced magnitude in sensor response as compared to the neat TPU/CB (EEL) composite, which was due to the disruption of the percolation pathway of carbon black (CB) by the addition of PVDF and $BaTiO_3$.

According to the cyclic voltammetry (CV) curves, the presence of the TPU/CB (EEL) matrix caused an increase in hysteresis for each cycle for all sensors. The progressive improvement of the electrical conductivity was likely due to the establishment of parallel circuits within the percolation pathway. Chronoamperometry scans in both the finger press and standardised impact force test configurations demonstrated that the current baseline and waveform amplitudes were maximised in the P4 sensors, which received both treatments (i.e., milling of $BaTiO_3$ and addition of TPPC). To illustrate, in the 0° direction, P4 sensors registered current baselines of 21.8 μA compared with untreated P1 sensors that had 0.0346 μA. There was also a consistent increase in current amplitudes from 0.328 μA to 32.2 μA from P1 to P4, increasing by two orders of magnitude in sensor output. This was attributed to the mechanical activation, namely to the surface texturing of the $BaTiO_3$ particles. Meanwhile, the addition of TPPC reduced the average size and improved the dispersion of the PVDF domains in the TPU matrix. This helped to preserve the spatial continuity and hence the electrical conductivity of the CB pathway.

Significant electrical anisotropy was also demonstrated for all sensors by means of the novel PCB board design, with the highest electrical response registered parallel to the printed infill however, this was only apparent during the finger press test. This was mainly attributed to the PVDF domains being preferentially aligned parallel to the rasters (printing direction) because of the shear forces imposed during the printing process. Electrical anisotropy may not be evident upon sudden application of pressure, such as the impact test.

Since the Curie temperature of $BaTiO_3$ was exceeded while extruding and printing, and PVDF mainly crystallised in the α polymorph, none of the sensors demonstrated significant piezoelectric properties. However, the improved performance achieved after milling $BaTiO_3$ and adding TPPC suggests that these treatments may be useful to achieve the desired piezoelectric configurations under a much lower poling potential as compared to conventional piezoelectric filaments. Future work will thus investigate in situ electrical poling under mild conditions to re-establish the piezoelectric character of the $BaTiO_3$ and PVDF inclusions for improved sensitivity and signal-to-noise ratio of the FFF sensors.

CRediT authorship contribution statement

Pejak Simunec Dejana: Writing – review & editing, Writing – original draft, Methodology, Investigation, Formal analysis, Data curation, Conceptualization. **Breedon Michael:** Writing – review & editing, Methodology, Formal analysis, Conceptualization. **Muhammad Faizan U.R.:** Methodology. **Kyratzis Louis:** Writing – review & editing. **Sola Antonella:** Writing – review & editing, Methodology, Investigation, Formal analysis.

Declaration of Competing Interest

The authors declare that they have no known competing financial interests or personal relationships that could have appeared to influence the work reported in this paper.

Data Availability

Data will be made available on request.

Acknowledgements

We kindly thank Arkema for their donation of Kynar 740. We also thank the Materials Characterisation and Modelling Program at CSIRO, specifically Sherman Wong for running the XRD scans, Yesim Gozukara and Mark Hickey for running the TGA and DSC scans and Microscopy Facility (Mark Greaves and Malisja de Vries). We also thank Sally Johnson for her assistance in preparing the PCB boards. DPS and AS are supported by CSIRO Research Office through the "Science Leader in Active Materials" program.

Appendix A. Supporting information

Supplementary data associated with this article can be found in the online version at doi:10.1016/j.addma.2023.103679.

References

[1] D. Xiang, Z. Zhang, Y. Wu, J. Shen, E. Harkin-Jones, Z. Li, P. Wang, C. Zhao, H. Li, Y. Li, 3D-printed flexible piezoresistive sensors for stretching and out-of-plane forces, Macromol. Mater. Eng. 306 (2021) 2100437, https://doi.org/10.1002/mame.202100437.

[2] A. Kumar, Methods and materials for smart manufacturing: additive manufacturing, internet of things, flexible sensors and soft robotics, Manuf. Lett. 15 (2018) 122–125, https://doi.org/10.1016/j.mfglet.2017.12.014.

[3] D. Xiang, X. Zhang, E. Harkin-Jones, W. Zhu, Z. Zhou, Y. Shen, Y. Li, C. Zhao, P. Wang, Synergistic effects of hybrid conductive nanofillers on the performance of 3D printed highly elastic strain sensors, Compos Part A Appl. Sci. Manuf. 129 (2020), 105730, https://doi.org/10.1016/j.compositesa.2019.105730.

[4] D. Xiang, X. Zhang, Y. Li, E. Harkin-Jones, Y. Zheng, L. Wang, C. Zhao, P. Wang, Enhanced performance of 3D printed highly elastic strain sensors of carbon nanotube/thermoplastic polyurethane nanocomposites via non-covalent interactions, Compos B Eng. 176 (2019), 107250, https://doi.org/10.1016/J.COMPOSITESB.2019.107250.

[5] D. Xiang, Z. Zhang, Z. Han, X. Zhang, Z. Zhou, J. Zhang, X. Luo, P. Wang, C. Zhao, Y. Li, Effects of non-covalent interactions on the properties of 3D printed flexible piezoresistive strain sensors of conductive polymer composites, Compos Interfaces 28 (2020) 1–15, https://doi.org/10.1080/09276440.2020.1794479.

[6] I. Kim, Y. Chae, S. Jo, D. Kim, Levitating oscillator-based triboelectric nanogenerator for harvesting from rotational motion and sensing seismic oscillation, Nano Energy 72 (2020), 104674, https://doi.org/10.1016/j.nanoen.2020.104674.

[7] G. Liu, Y. Gao, S. Xu, T. Bu, Y. Xie, C. Xu, H. Zhou, Y. Qi, C. Zhang, One-stop fabrication of triboelectric nanogenerator based on 3D printing, EcoMat 3 (2021), e12130, https://doi.org/10.1002/eom2.12130.

[8] A.Z. Stefanov, L.D. Zivanov, M.G. Kisic, A.B. Menicanin, Fully FFF-printed capacitive displacement sensor based on graphene/PLA composite and thermoplastic elastomer filaments, IEEE Sens J. 22 (2022) 10437–10445, https://doi.org/10.1109/JSEN.2022.3168931.

[9] G. Shen, Recent advances of flexible sensors for biomedical applications, Prog. Nat. Sci.: Mater. Int. 31 (2021) 872–882, https://doi.org/10.1016/j.pnsc.2021.10.005.

[10] D. Chen, Q. Pei, Electronic muscles and skins: a review of soft sensors and actuators, Chem. Rev. 117 (2017) 11239–11268, https://doi.org/10.1021/acs.chemrev.7b00019.

[11] Y. Khan, M. Garg, Q. Gui, M. Schadt, A. Gaikwad, D. Han, N.A.D. Yamamoto, P. Hart, R. Welte, W. Wilson, S. Czarnecki, M. Poliks, Z. Jin, K. Ghose, F. Egitto, J. Turner, A.C. Arias, Flexible hybrid electronics: direct interfacing of soft and hard electronics for wearable health monitoring, Adv. Funct. Mater. 26 (2016) 8764–8775, https://doi.org/10.1002/adfm.201603763.

[12] M. Mehrali, S. Bagherifard, M. Akbari, A. Thakur, B. Mirani, M. Mehrali, M. Hasany, G. Orive, P. Das, J. Emneus, T.L. Andresen, A. Dolatshahi-Pirouz, Blending electronics with the human body: a pathway toward a cybernetic future, Adv. Sci. 5 (2018) 1700931, https://doi.org/10.1002/advs.201700931.

[13] C.W. Foster, M.P. Down, Y. Zhang, X. Ji, S.J. Rowley-Neale, G.C. Smith, P.J. Kelly, C.E. Banks, 3D printed graphene based energy storage devices, Sci. Rep. 7 (2017) 1–11, https://doi.org/10.1038/srep42233.

[14] D. Xiang, X. Zhang, Z. Han, Z. Zhang, Z. Zhou, E. Harkin-Jones, J. Zhang, X. Luo, P. Wang, C. Zhao, Y. Li, 3D printed high-performance flexible strain sensors based on carbon nanotube and graphene nanoplatelet filled polymer composites, J. Mater. Sci. 55 (2020) 15769–15786, https://doi.org/10.1007/s10853-020-05137-w.

[15] B. Khatri, K. Lappe, M. Habedank, T. Mueller, C. Megnin, T. Hanemann, Fused deposition modeling of ABS-barium titanate composites: a simple route towards tailored dielectric devices, Polymers 10 (2018), https://doi.org/10.3390/polym10060666.

[16] X. Li, D. Ji, B. Yu, R. Ghosh, J. He, X. Qin, S. Ramakrishna, Boosting piezoelectric and triboelectric effects of PVDF nanofiber through carbon-coated piezoelectric nanoparticles for highly sensitive wearable sensors, Chem. Eng. J. 426 (2021), 130345, https://doi.org/10.1016/j.cej.2021.130345.

[17] T. Sebastian, M. Bach, A. Geiger, T. Lusiola, L. Kozielski, F. Clemens, Investigation of electromechanical properties on 3-D printed piezoelectric composite scaffold structures, Materials 14 (2021), https://doi.org/10.3390/MA14205927.

[18] K.B. Mustapha, K.M. Metwalli, A.A. Bin Baharuddin, Y. Abakr, 3D printing of polyvinylidene fluoride composite films with enhanced electroactive beta-phase for flexible wearable pressure sensors, Mater. Today Proc. (2022) 245, https://doi.org/10.1016/j.matpr.2022.09.245.

[19] H. Li, S.W. Jin, J.H. Lim, S. Lim, Solvent-assisted precipitation direct-write printing toward in-suit oriented β-phase polyvinylidene fluoride with tunable microarchitectures for energy harvesting and self-powered sensing, Appl. Mater. Today 29 (2022), 101633, https://doi.org/10.1016/j.apmt.2022.101633.

[20] H. Li, S. Lim, High-performance piezoelectric nanogenerators featuring embedded organic nanodroplets for self-powered sensors, J. Mater. Chem. A Mater. 10 (2022) 14894–14905, https://doi.org/10.1039/d2ta02276a.

[21] H. Li, H. Song, M. Long, G. Saeed, S. Lim, Mortise-tenon joint structured hydrophobic surface-functionalized barium titanate/polyvinylidene fluoride nanocomposites for printed self-powered wearable sensors, Nanoscale 13 (2021) 2542–2555, https://doi.org/10.1039/d0nr07525f.

[22] S. Bodkhe, G. Turcot, F.P. Gosselin, D. Therriault, One-step solvent evaporation-assisted 3D printing of piezoelectric PVDF nanocomposite structures, ACS Appl. Mater. Interfaces 9 (2017) 20833–20842, https://doi.org/10.1021/ACSAMI.7B04095/ASSET/IMAGES/LARGE/AM-2017-04095D_0009.JPEG.

[23] M. Marandi, J. Tarbutton, Additive manufacturing of single- And double-layer piezoelectric PVDF-TrFE copolymer sensors. Procedia Manuf, Elsevier, 2019, pp. 666–671, https://doi.org/10.1016/j.promfg.2019.06.194.

[24] B. Khatri, K. Lappe, M. Habedank, T. Mueller, C. Megnin, T. Hanemann, Fused deposition modeling of ABS-barium titanate composites: a simple route towards tailored dielectric devices, Polym. (Basel) 10 (2018) 2474–2482, https://doi.org/10.3390/polym10060666.

[25] Arkema Technical Polymers, MSDS - Kynar® 460 - Polyvinylidenefluoride (PVDF), (2022). https://matmatch.com/materials/arke0062-kynar-460?retired=Kynar® 460 (accessed November 1, 2022).

[26] X. Liu, Y. Shang, J. Liu, Z. Shao, C. Zhang, 3D printing-enabled in-situ orientation of BaTi2O5Nanorods in β-PVDF for high-efficiency piezoelectric energy harvesters, ACS Appl. Mater. Interfaces 14 (2022) 13361–13368, https://doi.org/10.1021/acsami.2c00443.

[27] H. Kim, F. Torres, Y. Wu, D. Villagran, Y. Lin, T.-L. Tseng, Integrated 3D printing and corona poling process of PVDF piezoelectric films for pressure sensor application, Smart Mater. Struct. 26 (2017), 085027, https://doi.org/10.1088/1361-665x/aa738e.

[28] J. Guo, M. Nie, Q. Wang, Self-poling polyvinylidene fluoride-based piezoelectric energy harvester featuring highly oriented β-phase structured at multiple scales, ACS Sustain Chem. Eng. 9 (2021) 499–509, https://doi.org/10.1021/acssuschemeng.0c07802.

[29] H. Pei, Y. Xie, Y. Xiong, Q. Lv, Y. Chen, A novel polarization-free 3D printing strategy for fabrication of poly (Vinylidene fluoride) based nanocomposite piezoelectric energy harvester, Compos B Eng. 225 (2021), 109312, https://doi.org/10.1016/j.compositesb.2021.109312.

[30] H. Pei, S. Shi, Y. Chen, Y. Xiong, Q. Lv, Combining solid-state shear milling and FFF 3D-printing strategy to fabricate high-performance biomimetic wearable fish-scale PVDF-based piezoelectric energy harvesters, ACS Appl. Mater. Interfaces 14 (2022) 15346–15359, https://doi.org/10.1021/acsami.2c02491.

[31] R. Sahoo, S. Mishra, L. Unnikrishnan, S. Mohanty, S. Mahapatra, S.K. Nayak, S. Anwar, A. Ramadoss, Enhanced dielectric and piezoelectric properties of Fe-doped ZnO/PVDF-TrFE composite films, Mater. Sci. Semicond. Process 117 (2020), 105173, https://doi.org/10.1016/j.mssp.2020.105173.

[32] H. Zhang, F. Ke, J. Shao, C. Wang, H. Wang, Y. Chen, One-step fabrication of highly sensitive pressure sensor by all FDM printing, Compos Sci. Technol. 226 (2022), 109531, https://doi.org/10.1016/j.compscitech.2022.109531.

[33] R. Patil, A. Ashwin, S. Radhakrishnan, Novel polyaniline/PVDF/BaTiO3 hybrid composites with high piezo-sensitivity, Sens Actuators A Phys. 138 (2007) 361–365, https://doi.org/10.1016/J.SNA.2007.05.025.

[34] NinjaTek, Safety Data Sheet SDS: EEL 3D Filament, (2018) 1–6.

[35] Inframat Advanced Materials, Barium Titanate Nano Powder Product # 5622ON-01, MSDS. (n.d.). http://www.advancedmaterials.us/5622ON-01.htm (accessed November 2, 2022).

[36] N. Awanis Hashim, Y. Liu, K. Li, Stability of PVDF hollow fibre membranes in sodium hydroxide aqueous solution, Chem. Eng. Sci. 66 (2011) 1565–1575, https://doi.org/10.1016/j.ces.2010.12.019.

[37] X. Liu, M. Mwangi, X. Li, M. O'Brien, G.M. Whitesides, Paper-based piezoresistive MEMS sensors, Lab Chip 11 (2011) 2189–2196, https://doi.org/10.1039/c1lc20161a.

[38] Voltage-Current Characteristics and Nonlinearities - Digilent Reference, Diligent Reference. (2022). https://digilent.com/reference/learn/fundamentals/circuits/voltage-current-characteristics/start (accessed December 10, 2022).
[39] N. Probst, Conducting carbon black. Carbon Black, Routledge, 2018, pp. 271–288, https://doi.org/10.1201/9781315138763-8.
[40] X. Ji, H. Li, D. Hui, K.T. Hsiao, J. Ou, A.K.T. Lau, I-V characteristics and electro-mechanical response of different carbon black/epoxy composites, Compos B Eng. 41 (2010) 25–32, https://doi.org/10.1016/j.compositesb.2009.05.001.
[41] M.Q. Zhang, H.M. Zeng, H.F. Wang, X. Yao, An equivalent circuit model for electric conductive polymer composites, 096369359300200, Adv. Compos. Lett. 2 (1993), https://doi.org/10.1177/096369359300200404.
[42] Z. Xie, Y.J. Yum, Simulation of carbon black network in filled rubber, J. Macromol. Sci., Part B: Phys. 46 B (2007) 403–410, https://doi.org/10.1080/00222340601158258.
[43] T. Košir, J. Slavič, Single-process fused filament fabrication 3D-printed high-sensitivity dynamic piezoelectric sensor, Addit. Manuf. 49 (2022), 102482, https://doi.org/10.1016/j.addma.2021.102482.
[44] A. Dijkshoorn, M. Schouten, S. Stramigioli, G. Krijnen, Modelling of anisotropic electrical conduction in layered structures 3d-printed with fused deposition modelling, Sensors 21 (2021) 3710, https://doi.org/10.3390/s21113710.
[45] D. Pejak Simunec, A. Sola, Emerging research in conductive materials for fused filament fabrication: a critical review, Adv. Eng. Mater. 24 (2022) 2101476, https://doi.org/10.1002/ADEM.202101476.
[46] A. Abdalla, H.H. Hamzah, O. Keattch, D. Covill, B.A. Patel, Augmentation of conductive pathways in carbon black/PLA 3D-printed electrodes achieved through varying printing parameters, Electro Acta 354 (2020), 136618, https://doi.org/10.1016/J.ELECTACTA.2020.136618.
[47] P. Martins, A.C. Lopes, S. Lanceros-Mendez, Electroactive phases of poly (vinylidene fluoride): determination, processing and applications, Prog. Polym. Sci. 39 (2014) 683–706, https://doi.org/10.1016/j.progpolymsci.2013.07.006.
[48] S. Bodkhe, G. Turcot, F.P. Gosselin, D. Therriault, One-step solvent evaporation-assisted 3D printing of piezoelectric PVDF nanocomposite structures, ACS Appl. Mater. Interfaces 9 (2017) 20833–20842, https://doi.org/10.1021/acsami.7b04095.
[49] T. Košir, J. Slavič, Single-process fused filament fabrication 3D-printed high-sensitivity dynamic piezoelectric sensor, Addit. Manuf. 49 (2022), 102482, https://doi.org/10.1016/j.addma.2021.102482.
[50] S. Sukumaran, S. Chatbouri, D. Rouxel, E. Tisserand, F. Thiebaud, T. Ben Zineb, Recent advances in flexible PVDF based piezoelectric polymer devices for energy harvesting applications, J. Intell. Mater. Syst. Struct. 32 (2021) 746–780, https://doi.org/10.1177/1045389X20966058.
[51] C. Fu, X. Wang, J. Qian, X. Ran, The correlation between crystallization kinetics and polymorphism behavior in the nanocomposite of poly(vinylidene fluoride) and quaternary phosphonium salts, Phys. Status Solidi (A) Appl. Mater. Sci. 214 (2017) 1–12, https://doi.org/10.1002/pssa.201600869.
[52] S.J. Kang, Y.J. Park, J. Sung, P.S. Jo, C. Park, K.J. Kim, B.O. Cho, Spin cast ferroelectric beta poly(vinylidene fluoride) thin films via rapid thermal annealing, Appl. Phys. Lett. 92 (2008), 012921, https://doi.org/10.1063/1.2830701.
[53] N. Khan, H. Omran, Y. Yao, K.N. Salama, Flexible PVDF ferroelectric capacitive temperature sensor. Midwest Symposium on Circuits and Systems, Institute of Electrical and Electronics Engineers Inc., 2015, https://doi.org/10.1109/MWSCAS.2015.7282063.
[54] G. Jones, R. Assink, T. Dargaville, P. Chaplya, R. Clough, J. Elliott, J. Martin, D. Mowery, M. Celina, Characterization, performance and optimization of PVDF as a piezoelectric film for advanced space mirror concepts, Albuquerque (2005).
[55] Y. Cho, J. Jeong, M. Choi, G. Baek, S. Park, H. Choi, S. Ahn, S. Cha, T. Kim, D. S. Kang, J. Bae, J.J. Park, BaTiO3@PVDF-TrFE nanocomposites with efficient orientation prepared via phase separation nano-coating method for piezoelectric performance improvement and application to 3D-PENG, Chem. Eng. J. 427 (2022), 131030, https://doi.org/10.1016/j.cej.2021.131030.
[56] I.-W. Chen, Dielectric and ferroelectric ceramics: interfaces. Encyclopedia of Materials: Science and Technology, Elsevier, 2001, pp. 2152–2157, https://doi.org/10.1016/b0-08-043152-6/00388-0.
[57] N. Jia, Q. Xing, X. Liu, J. Sun, G. Xia, W. Huang, R. Song, Enhanced electroactive and mechanical properties of poly(vinylidene fluoride) by controlling crystallization and interfacial interactions with low loading polydopamine coated BaTiO3, J. Colloid Interface Sci. 453 (2015) 169–176, https://doi.org/10.1016/j.jcis.2015.05.002.
[58] X. Li, H. Hu, T. Hua, B. Xu, S. Jiang, Wearable strain sensing textile based on one-dimensional stretchable and weavable yarn sensors, Nano Res 11 (2018) 5799–5811, https://doi.org/10.1007/S12274-018-2043-7/METRICS.
[59] R. Tao, J. Shi, M. Rafiee, A. Akbarzadeh, D. Therriault, Fused filament fabrication of PVDF films for piezoelectric sensing and energy harvesting applications, Mater. Adv. 3 (2022) 4851–4860, https://doi.org/10.1039/d2ma00072e.
[60] J. Cheng, S. Wang, S. Chen, J. Zhang, X. Wang, Properties and crystallization behavior of poly (vinylidene fluoride) (PVDF)/thermoplastic polyurethane elastomer (TPU) blends, Desalin. Water Treat. 34 (2011) 184–189, https://doi.org/10.5004/DWT.2011.2791.
[61] Q. Zhang, J. Wang, J. Yu, Z.X. Guo, Improved electrical conductivity of TPU/carbon black composites by addition of COPA and selective localization of carbon black at the interface of sea-island structured polymer blends, Soft Matter 13 (2017) 3431–3439, https://doi.org/10.1039/C7SM00346C.
[62] M.S. Sorayani Bafqi, R. Bagherzadeh, M. Latifi, Fabrication of composite PVDF-ZnO nanofiber mats by electrospinning for energy scavenging application with enhanced efficiency, J. Polym. Res. 22 (2015) 1–9, https://doi.org/10.1007/s10965-015-0765-8.
[63] F. Mokhtari, J. Foroughi, M. Latifi, Enhancing β crystal phase content in electrospun PVDF nanofibers, in: Energy Harvesting Properties of Electrospun Nanofibers, IOP Publishing, 2019, pp. 1–28, https://doi.org/10.1088/978-0-7503-2005-4ch5.
[64] H. Zhang, Y. Zhu, L. Li, Fabrication of PVDF/graphene composites with enhanced β phase: Via conventional melt processing assisted by solid state shear milling technology, RSC Adv. 10 (2020) 3391–3401, https://doi.org/10.1039/c9ra09459h.
[65] R. Gregorio, Determination of the α, β, and γ crystalline phases of poly(vinylidene fluoride) films prepared at different conditions, J. Appl. Polym. Sci. 100 (2006) 3272–3279, https://doi.org/10.1002/app.23137.
[66] S. Dashtizad, P. Alizadeh, A. Yourdkhani, Improving piezoelectric properties of PVDF fibers by compositing with BaTiO3-Ag particles prepared by sol-gel method and photochemical reaction, J. Alloy. Compd. 883 (2021), 160810, https://doi.org/10.1016/j.jallcom.2021.160810.
[67] S.F. Mendes, C.M. Costa, C. Caparros, V. Sencadas, S. Lanceros-Méndez, Effect of filler size and concentration on the structure and properties of poly(vinylidene fluoride)/BaTiO 3 nanocomposites, J. Mater. Sci. 47 (2012) 1378–1388, https://doi.org/10.1007/s10853-011-5916-7.
[68] H. Kim, T. Fernando, M. Li, Y. Lin, T.L.B. Tseng, Fabrication and characterization of 3D printed BaTiO3/PVDF nanocomposites, J. Compos Mater. 52 (2018) 197–206, https://doi.org/10.1177/0021998317704709.
[69] D.H. Yoon, Tetragonality of barium titanate powder for a ceramic capacitor application, J. Ceram. Process. Res. 7 (2006) 343–354.
[70] M. Acosta, N. Novak, V. Rojas, S. Patel, R. Vaish, J. Koruza, G.A. Rossetti, J. Rödel, BaTiO3-based piezoelectrics: Fundamentals, current status, and perspectives, Appl. Phys. Rev. 4 (2017), 041305, https://doi.org/10.1063/1.4990046.
[71] H. Abdolmaleki, S. Agarwala, PVDF-batio3 nanocomposite inkjet inks with enhanced β-phase crystallinity for printed electronics, Polymers 12 (2020) 1–12, https://doi.org/10.3390/polym12102430.
[72] J. González-Benito, D. Olmos, J.M. Martínez-Tarifa, G. González-Gaitano, F. A. Sánchez, PVDF/BaTiO 3 /carbon nanotubes ternary nanocomposites prepared by ball milling: Piezo and dielectric responses, J. Appl. Polym. Sci. 136 (2019) 47788, https://doi.org/10.1002/app.47788.
[73] H.J. Oh, D.K. Kim, Y.C. Choi, S.J. Lim, J.B. Jeong, J.H. Ko, W.G. Hahm, S.W. Kim, Y. Lee, H. Kim, B.J. Yeang, Fabrication of piezoelectric poly(l-lactic acid)/BaTiO3 fibre by the melt-spinning process, Sci. Rep. 10 (2020) 1–12, https://doi.org/10.1038/s41598-020-73261-3.
[74] H. Liu, M. Dong, W. Huang, J. Gao, K. Dai, J. Guo, G. Zheng, C. Liu, C. Shen, Z. Guo, Lightweight conductive graphene/thermoplastic polyurethane foams with ultrahigh compressibility for piezoresistive sensing, J. Mater. Chem. C. Mater. 5 (2017) 73–83, https://doi.org/10.1039/c6tc03713e.
[75] M. Dong, Q. Li, H. Liu, C. Liu, E.K. Wujcik, Q. Shao, T. Ding, X. Mai, C. Shen, Z. Guo, Thermoplastic polyurethane-carbon black nanocomposite coating: Fabrication and solid particle erosion resistance, Polym. (Guildf.) 158 (2018) 381–390, https://doi.org/10.1016/j.polymer.2018.11.003.
[76] W. Li, H. Li, Y.M. Zhang, Preparation and investigation of PVDF/PMMA/TiO2 composite film, J. Mater. Sci. 44 (2009) 2977–2984, https://doi.org/10.1007/s10853-009-3395-x.
[77] H. Koerner, W. Liu, M. Alexander, P. Mirau, H. Dowty, R.A. Vaia, Deformation-morphology correlations in electrically conductive carbon nanotube - thermoplastic polyurethane nanocomposites, Polym. (Guildf.) 46 (2005) 4405–4420, https://doi.org/10.1016/j.polymer.2005.02.025.
[78] G.M. Wallner, Z. Major, G.A. Maier, R.W. Lang, Fracture analysis of annealed PVDF films, Polym. Test. 27 (2008) 392–402, https://doi.org/10.1016/j.polymertesting.2008.01.006.
[79] C. Fu, X. Wang, J. Qian, X. Ran, The correlation between crystallization kinetics and polymorphism behavior in the nanocomposite of poly(vinylidene fluoride) and quaternary phosphonium salts, Phys. Status Solidi (A) Appl. Mater. Sci. 214 (2017) 1600869, https://doi.org/10.1002/pssa.201600869.
[80] Z. Fan, M. Schwedes, J. Schwaderer, S. Beuermann, M. Fischlschweiger, Molecular weight as a key for electroactive phase formation in poly(vinylidene fluoride, Mater. Res Lett. 10 (2022) 271–277, https://doi.org/10.1080/21663831.2022.2036840.
[81] A. Moghtada, A. Heidary Moghadam, R. Ashiri, Tetragonality enhancement in BaTiO3 by mechanical activation of the starting BaCO3 and TiO2 powders: characterization of the contribution of the mechanical activation and postmilling calcination phenomena, Int J. Appl. Ceram. Technol. 15 (2018) 1518–1531, https://doi.org/10.1111/ijac.13019.
[82] V.P. Pavlović, J. Krstić, M.J. Šćepanović, J. Dojčilović, D.M. Minić, J. Blanuša, S. Stevanović, V. Mitić, V.B. Pavlović, Structural investigation of mechanically activated nanocrystalline BaTiO3 powders, Ceram. Int 37 (2011) 2513–2518, https://doi.org/10.1016/j.ceramint.2011.03.064.